UNIVERSITAT ROVIRA I VIRGILI

DEEEA
Departament d'Enginyeria Electrònica, Elèctrica i Automàtica

Ph. D. STUDENTS WORKSHOP

on

ELECTRONIC ENGINEERING

Tarragona, June 26-27, 2006

Abstracts Book

Ph. D. Students Workshop

on

Electronic Engineering

Tarragona, June 26-27, 2006

Organising Comitee

Josep Pallares Marzal

Lluis F. Marsal Garvi

Josep Ferré Borrull

Anna Beltran Ras

Margarita Rebenaque Esteve

Schedule

Monday, 26th June

10:00 Plenary session 1

11:00 Coffee break

11:30 Plenary session 2

13:00 Lunch

14:45 Plenary session 3

16:30 Poster Session 1

Tuesday, 27th June

10:00 Plenary session 4

11:00 Coffee break

11:30 Plenary session 5

13:00 Lunch

14:45 Plenary session 6

16:00 Poster session 2

17:00 Best Poster Award and Closing sesion

Invited Speakers

Plenary sesion 1

SOI devices and materials overview for Nanoscale CMOS

Prof. Francis Balestra
Institut de Microélectronique, Electromagnétisme et Photonique,
IMEP (CNRS-INPG-UJF), INP Grenoble-Minatec

Plenary sesion 2

Compact Modeling of Short-Channel Nanoscale Double Gate and Gate-All-Around MOSFET's Using Conformal Mapping Techniques

Prof. Tor Fjeldly
Unik, Kjeller, Norway

Plenary sesion 3

Inorganic and organic TFTs: Fabrication and Modeling

Prof. Magali Estrada del Cueto
Centro de Investigación y de Estudios Avanzados del IPN, México D.F.
Departamento de Ingeniería Eléctrica
Sección de Electrónica del Estado Sólido

Plenary sesion 4

El curioso incidente de la oveja a medianoche

Prof. Julie Wilson
York Structural Biology Laboratory. Department of Chemistry
University of York

Plenary sesion 5

The Role of METABO*OMICS in Biomedicine: 1H NMR Spectroscopy in Disease Risk Assessment and Diagnostics

Prof. Mika Ala-Korpela
Laboratory of Computational Engineering, Systems Biology and Bioinformation Technology, Helsinki University of Technology

Plenary sesion 6

Spectroscopic Ellipsometry and Polarimetry for optical characterization of surfaces, interfaces and thin films

Prof. Enric Garcia-Caurel
Laboratoire de Physique des Interfaces et Couches Minces.
CNRS-École Polytechnique. Paris.

Index

Invited Speakers

Posters

Plenary Sessions

SOI devices and materials overview for Nanoscale CMOS

Prof. Francis Balestra

Institut de Microélectronique, Electromagnétisme et Photonique,
IMEP (CNRS-INPG-UJF), INP Grenoble-Minatec
balestra@enserg.fr

A review of recently explored new effects in SOI nanodevices and materials is given. Recent advances in the understanding of the sensitivity of electron and hole transport to the tensile or compressive uniaxial and biaxial strains in thin film SOI are presented. The performance and physical mechanisms are also addressed in multi-gate Si, SiGe and Ge MOSFETs. The impact of gate misalignment or underlap, as well as the use of the back gate for charge storage in double-gate nanodevices and of capacitorless DRAM are also outlined.

Compact Modeling of Short-Channel Nanoscale Double Gate and Gate-All-Around MOSFET's Using Conformal Mapping Techniques

Prof. Tor Fjeldly

Unik, Kjeller, Norway
torfj@unik.no

A modeling framework for short-channel double gate and cylindrical gate-all-around MOSFETs are presented. The device electrostatics in the subthreshold regime of both is dominated by the capacitive coupling between the electrodes. In the DG, the potential variation is analyzed in terms of conformal mapping techniques. Accounting for the difference in gate control between DG and GAA MOSFET, we show that the 2D potential distribution of the DG device can be mapped into the cross-section through the cylinder axis of the GAA device. In the strong inversion regime, the device behavior is dominated by the inversion charge, permitting the use of a 1D analysis. The present models are verified by comparison with numerical device simulations both for the electrostatics and for the drain current.

Inorganic and organic TFTs: Fabrication and Modeling

Prof. Magali Estrada del Cueto

Centro de Investigación y de Estudios Avanzados del IPN, México D.F.
Departamento de Ingeniería Eléctrica, Sección de Electrónica del Estado Sólido
mestrada@cinvestav.mx

This presentation reviews important moments in the development of inorganic and organic TFTs regarding their fabrication, physics and modeling. First results in the fabrication of a-Si 1-x C x TFTs and the changes in their electrical characteristics after crystallization by Excimer Laser Annealing will be shown. Details of a unified model and parameter extraction method, UMEM, that has been successfully applied to amorphous, nanocrystalline and polycrystalline inorganic TFTs, as well as to organic, (pentacene), TFTs will also be summarized.

El curioso incidente de la oveja a medianoche

Prof. Julie Wilson

York Structural Biology Laboratory. Department of Chemistry, University of York
julie@ysbl.york.ac.uk

Metabolomics seeks to provide a comprehensive profile of all metabolites present in a sample by analysis of physio-chemical data. Metabolic fingerprinting approaches have recently emerged as a non-biased alternative to the determination of individual levels of a specific metabolite or class of metabolites in large sets of samples, as is necessary for clinical diagnosis purposes. 1 H-Nuclear Magnetic Resonance (1 H-NMR) is a highly reproducible method and has been widely used in the search for disease biomarkers whereas capillary electrophoresis (CE) has not yet been fully exploited in a non-targeted approach. Both methods produce highly complex data sets and require multivariate techniques for interpretation. Characteristic features in the data can be used in pattern recognition methods for classification but, before these can be applied, pre-processing is required to remove the influence of different instrumental factors. Most importantly, the data need to be aligned correctly before direct comparisons can be made. The importance of experimental design will become apparent in this presentation!

THE ROLE OF METABO*OMICS IN BIOMEDICINE: ^{1}H NMR SPECTROSCOPY IN DISEASE RISK ASSESSMENT AND DIAGNOSTICS

Mika Ala-Korpela

Laboratory of Computational Engineering, Systems Biology and Bioinformation Technology, Helsinki University of Technology, P.O.Box 9203, FI-02015 HUT, Espoo, Finland --- mika.ala-korpela@hut.fi

Abstract

Measuring metabolites is not new. For decades, clinicians have monitored chemistries in various body fluids, e.g., using glucose to track diabetes and cholesterol to screen heart disease. What is new in the metabo*omics approaches is that we are now attempting to collect an unbiased sample of metabolites that can serve as a snapshot of an organism's (patho)physiology. As an ultimate goal we wish to distinguish between an individual who is healthy and someone who has (diagnosis) – or might develop (risk assessment) – a disease.

1. Introduction

Mass and nuclear magnetic resonance (NMR) have become the two key spectroscopies applied in metabo*omics applications. An appealing feature of NMR for metabonomic applications is its specific yet non-selective nature: using ^{1}H NMR spectroscopy one can efficiently obtain information on a large number of metabolites in biological fluids like human serum [1]. Recently, a call for applying ^{1}H NMR metabonomics to facilitate disease risk assessment and clinical diagnostics has also emerged [2-4]. A key issue in bringing metabonomics for clinical use will be to bridge the gap between biochemistry – as revealed by ^{1}H NMR spectroscopy – and the relevant measures of current clinical practice.

2. Molecular Windows

As illustrated in Fig. 1 the ^{1}H NMR experiments of serum samples can be targeted at two different molecular windows – lipoprotein lipids (LIPO) and low-molecular-weight metabolites (LMWM). The assignments for the LIPO window resonances refer to fatty acids in triglycerides, cholesterol compounds and phospholipids in various lipoprotein particles, the cholesterol backbone $-C(18)H_3$ and the $-N(CH_3)_3$ groups of surface phospholipids. The LMWM resonances marked gp are from glycoproteins.

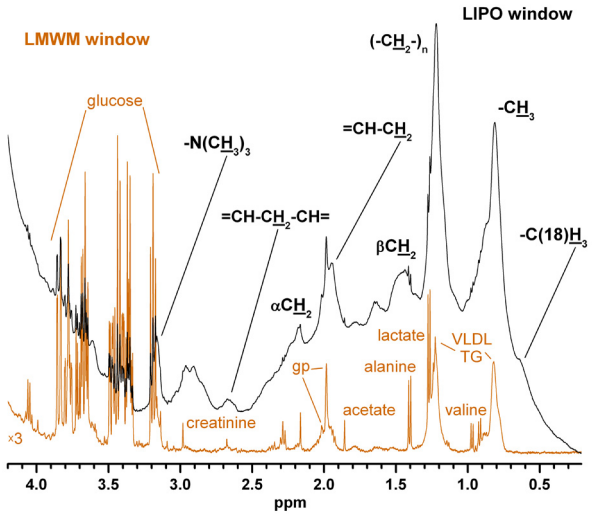

Fig. 1. Illustration of characteristic ^{1}H NMR molecular windows for a type 1 diabetic patient.

3. Characteristics and Analysis of Data

In a ^{1}H NMR spectrum, one metabolite can manifest several peaks, and the signal intensities are both biochemically and (patho)physiologically related. Furthermore, the data sets are extensive but redundant: one measurement can yield tens of thousands of data points, but the effective dimensionality is much less due to a smaller number of NMR-visible compounds. There is also heavy overlap of metabolite resonances [1,5]. For these reasons there are also methodological challenges in trying to associate ^{1}H NMR metabonomics data to diagnostically relevant biochemical variables. Two typical simplifications often made in handling the data are the use of 'bins', i.e., summed spectral intensities over fairly broad regions, and the application of rather uninformative chemometric methods, such as principal component analysis. This often hampers the biochemical rationale of the results. Here we will illustrate and apply a straightforward and visual approach facilitating the use of full spectral resolution

and allowing detection of intra- and inter-molecular dependencies in metabonomic data sets. The approach involves calculation of the correlation and covariance between all the data points in a data set and displaying the information in the form of colour-coded pseudo-2D NMR spectra.

4. Diagnostic Role in Diabetes

Recent literature [3,4] as well as our own work [5,6] point towards a key role for ^{1}H NMR spectroscopy in evaluating metabolic phenotypes for disease risk assessment and diagnostics. From our recent application [6] we will show how ^{1}H NMR metabonomics data – obtained in two molecular windows in a set of 182 type 1 diabetic patients – can be associated with key clinical measures by the aid of statistically significant correlation patterns. Furthermore, using various regression analyses, we will illustrate the quantitative nature of the metabolite information present in a ^{1}H NMR metabonomic data set of serum, not only for the well established case of lipoprotein lipids [1,5], but also for apolipoprotein components and for low-molecular-weight metabolites [6].

5. Fuzzy Pathophysiology

In many disease processes the biological heterogeneity as well as the potentially slow development and progression of pathological conditions make the borderline between 'healthy' and 'diseased' fuzzy (Fig. 2). Atherosclerosis is also a diffuse systemic disease, characterised by the local build-up of lipid-rich plaques within the walls of large arteries. The atherothrombotic processes are multigenetic, being influenced also by dietary and environmental components, and are apparent as early as the second decade in life with an increased incidence in the elderly. Atherothrombosis involves inflammatory processes with an array of metabolic, molecular and cellular manifestations in tissues, e.g., those depicted within the arterial wall. A varying degree of these intimal processes are reflected by the biochemistry of serum.

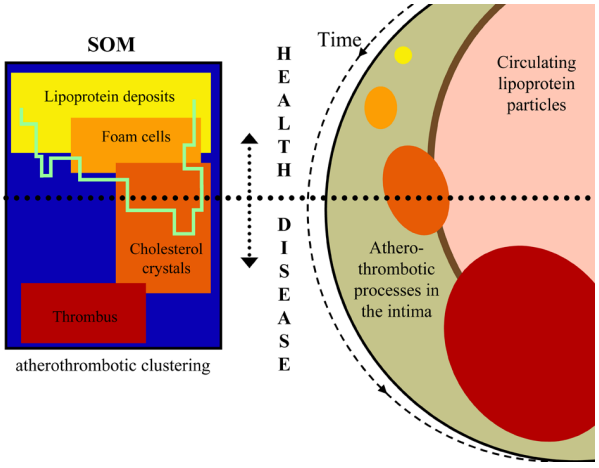

Fig. 2. A schematic simplification of the challenge related to the risk assessment and diagnosis of atherothrombosis.

One option to approach the problem, as studied and discussed in this presentation, is ^{1}H NMR metabonomics of serum equipped with a chemometric classifier, e.g., a self-organising map (SOM). On the left in Fig. 2 a hypothetical SOM is shown together with four overlapping clusters that are thought to represent the metabolic changes in the arterial intima. While definite classification as 'healthy' and 'diseased' may not be available by nature, the metabonomics approach with a holistic look at the multidimensional metabolic changes may prove useful in the assessment and follow up of individual 'health path' (represented by the light green line within the SOM) alongside the interplay between metabolic pathways and their consequences.

6. Conclusions

Development of metabonomic approaches, capable to visualise and interpret multidimensional metabolic influences rather than to try to find 'complete' classifications of 'health' and 'disease', is in our opinion a key for the favourable reception of ^{1}H NMR metabonomics in the clinical field. Generally, the high analytical power of the combined molecular windows gives additional confidence for the metabonomics approach and suggests realistic potential for the usage of ^{1}H NMR metabonomics also as an aid for disease diagnostics. Analysis approaches that indicate the biochemical rationale for the diagnostic outcome make the NMR metabonomics approach much more easily acceptable for the clinical arena as it would be without clear emphasis on the molecular biochemistry. The new analysis approaches and biomedical findings that will be presented are expected to stimulate discussions on the diagnostic potential of ^{1}H NMR spectroscopy and the important role of new data analysis methods in paving the way for ^{1}H NMR metabonomics into clinics.

References

[1] Ala-Korpela M (1995) ^{1}H NMR spectroscopy of human blood plasma. Progr Nucl Magn Reson Spectr 27:475-554.

[2] Griffin JL (2003) Metabonomics: NMR spectroscopy and pattern recognition analysis of body fluids and tissues for characterisation of xenobiotic toxicity and disease diagnosis. Curr Opin Chem Biol 7:648–54.

[3] Clayton TA, Lindon JC, Cloarec O, Antti H, Charuel C, Hanton G, Provost JP, Le Net JL, Baker D, Walley RJ, Everett JR, Nicholson JK (2006) Pharmaco-metabonomic phenotyping and personalized drug treatment. Nature 440:1073-7.

[4] Kirschenlohr HL, Griffin JL, Clarke SC, Rhydwen R, Grace AA, Schofield PM, Brindle KM, Metcalfe JC (2006) Proton NMR analysis of plasma is a weak predictor of coronary artery disease. Nat Med 12:705-10.

[5] Ala-Korpela M, Lankinen N, Salminen A, Suna T, Soininen P, Laatikainen R, Ingman P, Jauhiainen M, Taskinen MR, Héberger K, Kaski K (2006) The inherent accuracy of ^{1}H NMR spectroscopy to quantify plasma lipoproteins is subclass dependent. Atherosclerosis, in press.

[6] Mäkinen VP, Soininen P, Forsblom C, Parkkonen M, Ingman P, Kaski K, Groop PH, Ala-Korpela M (2006) Diagnosing diabetic nephropathy by ^{1}H NMR metabonomics of serum. Magn Reson Mater Phys Biol Med, submitted.

Spectroscopic Ellipsometry and Polarimetry for optical characterization of surfaces, interfaces and thin films

Prof. Enric Garcia-Caurel
Laboratoire de Physique des Interfaces et Couches Minces. CNRS-École Polytechnique. Paris.
garcia@poly.polytechnique.fr
http://www.lpicm.polytechnique.fr/pola/home.html

Conventional ellipsometry is a non-destructive optical characterization technique that has been widely used to the study of surfaces and interfaces. Its non destructive character, together with the possibility to perform real-time and in-situ analysis, have made ellipsometry ideal for process control in many industrial and research areas, and especially in the semiconductor sector. While perfectly planar and isotropic surfaces can be easily studied with ellipsometry, polarimetry is more convenient to the characterization of surfaces showing complex optical responses due to depolarization, roughness, or anisotropy among others. Polarimetry has been also successfully used in optical metrology to reconstruct the profile of diffraction gratings and other nano-sized objects. Because ellipsometry and polarimetry are based on the measurement of a phase difference, they show a high sensitivity that can be employed to detect extremely thin or even sub-monolayer films. Spectroscopic ellipsometric and polarimetric measurements can be performed in a spectral range spanning from the far ultraviolet, 9eV, to the mid infrared, 12 micron. This broad spectral accessibility, allows the exploration of the chemical composition, the structural conformation, as well as the physical structure of matter at different scales, going from the millimetre to the nanometre.

Posters

Gas detection with hybrid metal oxides/MWCNT and metal decorated MWCNT

E.H. Espinosa[1], R. Ionescu[1], B. Chambon[2], G. Bedis[2], C. Bittencourt[3], A. Felten[3], J-J. Pireaux[3] and E. Llobet[1]

[1] Universitat Rovira i Virgili, ETSE-DEEEA, Av. Països Catalans 26, E-43007 Tarragona, Spain
[2] Institut Univ. de Technologie GEII Bordeaux 1, 15 rue Naudet, 33175 Gradignan Cedex, France
[3] Falcultés Universitaires Notre Dame de la Paix, LISE, 61 rue de Bruxelles, B-5000 Namur, Belgium

Abstract

In this work we investigate the sensitivity of metal-decorated carbon nanotubes and mixed metal oxides (SnO_2 and WO_3) and functionalized multi wall carbon nanotubes (MWCNTs) to low concentrations of polluting gases (NO_2 and CO). We show that the gas detection at low operating temperatures can be considerably improved if using these sensitive materials.

1. Introduction

Worldwide concern of environmental safety imposes the monitoring of hazardous gas emission into the atmosphere. Combined with recent advances in wireless sensor networks, there is a need of developing low-cost sensing elements and low-power consumption gas sensors. In this frame, CNTs-based sensors can be a key device [1-2]. The good potential of CNTs for detecting gases arises from their very large surface area; moreover the possibility to tailor their surface reactivity by grafting functional groups can be used to improve their sensing properties. Metal atoms clustering on CNTs surfaces have been the subject of increased interest during the last few years, owing to the possibility of using the combination of these two nanostructures as a versatile building block for the construction of nanodevices [3].

In this work, we investigate the performances of hybrid gas sensors, made of O_2-functionalized MWCNT and two types of metal oxides (SnO_2 and WO_3), as well as the gas sensing properties at low operating temperatures of gas sensors based on Au- and Ag-decorated MWCNT previously functionalized in O_2 plasma.

2. Experimental

MWCNT grown by Chemical Vapor Deposition and functionalized in O_2 oxygen plasma were used as active layers in two different forms. Firstly, gold and silver metallic nanoclusters were grown on the surface of the carbon nanotubes by thermal evaporation, which ensured a good dispersion of the metallic nanoclusters. Secondly, hybrid materials were obtained by mixing functionalized MWCNTs with commercially available SnO_2 or WO_3 nanopowders (Sigma-Aldrich ®). These materials were got by adding 0.7 mg of oxygen functionalized MWCNT to 350 mg of a metal oxide (giving a proportion of 1/500 wt. %).

All materials produced were drop-coated over gas sensors substrates; glycerol, used as an organic vehicle, was added to the materials, and the resulting solutions were stirred in an ultrasonic bath at 75°C for 2 hours. The deposited sensing films were dried at 170ºC during 1 h in order to burn out the organic vehicle, and after that were annealed in situ at 400°C during 2 h in ambient atmosphere. During the annealing process, the temperature was raised from the ambient to 400°C using a ramp of 1 hour.

In total, six different types of active layers were produced. Specifically, depending on the metal oxide and power applied during MWCNTs functionalization (either 30 W or 100 W), they were:

- Sample A: SnO_2/MWCNTs (30 W)
- Sample B: SnO_2/MWCNTs (100 W)
- Sample C: WO_3/MWCNTs (30 W)
- Sample D: WO_3/MWCNTs (100 W)
- Sample E: Au- decorated MWCNTs (30 W)
- Sample F: Au- decorated MWCNTs (100 W)
- Sample G: Ag- decorated MWCNTs (30 W)
- Sample H: Ag- decorated MWCNTs (100 W)

The gas sensing properties of the different sensing films were tested in the presence of NO_2 and CO gases both at the ambient temperature and 150°C. Three concentrations of each gas under study were measured: 500 ppb, 1.5 and 6.5 ppm for NO_2, and 1, 10 and 50 ppm for CO. The sensors were placed inside an air tight 5.3 dm^3 measurement chamber, and the desired concentrations of the gases were introduced by the direct injection method. In order to assess the reproducibility of the results, each measurement was replicated four times.

3. Results and Discussion

TEM analyses (Figure 1) showed the formation of good shaped Au clusters on the carbon nanotubes walls and a homogeneous distribution of them.

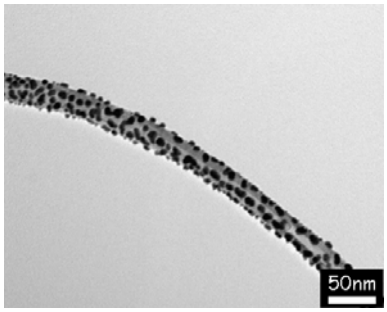

Fig.1. TEM image of Au-decorated O_2-functionalized MWCNT

For assessing sensors characteristics, the responsiveness was defined as the ratio between the change experienced in the sensor resistance after its exposure to a test gas and the sensor baseline resistance in air (eq 1).

$$S = \frac{|R_{air} - R_{gas}|}{R_{air}} \quad (1)$$

Typical responses of the Au- and Ag-decorated MWCNT gas sensors in the case of NO_2 test gas detection are shown in Figure 2. The changes experienced by the sensing materials resistance after their exposure to successive concentrations of NO_2 can be obviously observed. When operated at room temperature, the sensors needed approximately 20 minutes to reach a steady state after gas injection. This time was reduced by a factor of two when the sensors were operated at 150 ºC.

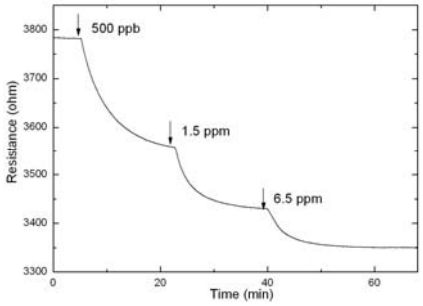

Fig.2. Resistance change to NO_2 experienced by sample E operated at ambient temperature

The detection of 500 ppb of NO_2 at room temperature was achieved by both differently metal-decorated MWCNT layers. Slightly better responsiveness was shown by the Au-decorated MWCNT. An important remark is that very similar results were obtained when the operation temperature of the gas sensors was raised to 150 ºC. No sensitivity of the sensors to CO test gas was found, as they presented a value of responsiveness just a little above 1 % only after the injection of 50 ppm of CO.

The most sensitive in the case of NO_2 detection have proved to be materials that used SnO_2 as metal oxide. They were able to detect as low as 500 ppb of this gas even at room temperature, with responsiveness near 20, similar values being obtained also when the sensors were operated at 150ºC. A typical sensor response to successive concentrations of NO_2 can be observed in Figure 3. An important remark is that similar sensors responsivenesses were obtained both at room temperature and 150ºC.

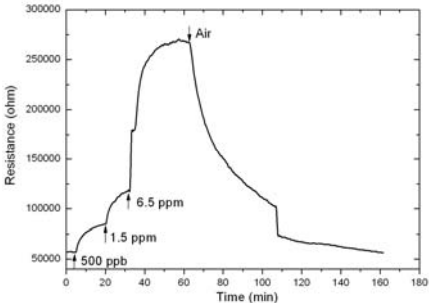

Figure 3. Response of Sample C operated at 150ºC to succesive concentrations of NO_2

CO measurements indicated again that better results are obtained when SnO_2 is used as metal oxide. Their response to this gas was, anyway, much lower than the one towards NO_2. Their responsiveness was near 13 in the presence of 50 ppm of CO when the sensors were operated at 150ºC. At room temperature their behavior to CO was even worse, their responsiveness decreasing below a value of 2. The sensors that employed WO_3 as metal oxide did not experience any change in their resistance after CO exposures.

4. Conclusions

Metal-decorated MWCNT were able to detect as low as 500 ppb of NO_2 even when operated at the ambient temperature or 150 ºC. Slightly superior results were obtained by sensors based on MWCNT covered with Au nanoclusters as compared with the ones covered with Ag nanoclusters.

The experimental results showed that samples using SnO_2 and WO_3 as metal oxides behave as n-type semiconductors since their resistance decreased in the presence of NO_2 (i.e., an oxidizing species), while samples with metal-decorated MWCNTS behave as p-type semiconductor. SnO_2 has proved to be the most suitable additive to nanotubes, presenting good results especially in the case of NO_2 detection at room temperature. This sensors show high sensitivity and good recovery after exposure to gases.

References

[1] C. Bittencourt et al, "WO3 films modified with functionalised multi-wall carbon nanotubes: Morphological, compositional and gas response studies", *Sensors and Actuators B*, pp. 33-41, 2006.

[2] R. Ionescu et al, "Oxygen functionalisation of MWNT and their use as gas sensitive thick-film layers", *Sensors and Actuators B*, pp. 36-46, 2006.

[3] C.C. Chien and K.T. Jeng, "Effective preparation of carbon nanotube-supported Pt–Ru electrocatalysts", *Materials Chemistry and Physics*, pp. 80-87, 2006.

Prevention of terrorist attacks: monitoring warfare precursors

E.H. Espinosa[1], R. Ionescu[1], A. Felten[2], C. Bittencourt[2], J.J. Pireaux[2], Z. Topalian[3], P. Heszler[3], C.G. Granqvist[3] and E. Llobet[1]

[1]Rovira i Virgili Univ., ETSE-DEEEiA, Av. Països Catalans 26, 43006 Tarragona, Spain
[2]Facultés Univ. Notre Dame de la Paix, LISE, 61 Rue de Bruxelles, 5000 Namur, Belgium
[3]Uppsala Univ., Ångström Laboratory, P.O. Box 534, 75121 Uppsala, Sweden

Abstract

With the detection of warfare precursors the European security is addressed. For this purpose we propose a method based on chemical gas sensors with superposed layers of multi-walled carbon nanotubes (MWCNT) and tungsten trioxide (WO_3) as active materials. Vapors of dymethyl. methylphosphonate (DMMP), precursor of the sarin gas, could be detected even when the sensors were operated at room temperature.

1. Introduction

Nowadays the European homeland security has unfortunately become an important issue due to a new type of menace in the world: terrorist attacks. Severely controls are realized to passengers passing through airport, and even to the ones traveling by trains, buses or other means of transport.

The sarin gas was developed in Germany during the 30's and is classified among the most dangerous chemical warfare agents. It is twenty times more deadly than cyanide gas. With this gas as protagonist, on March 20th, 1995, Tokyo suffered the most important terrorist attack in Japanese history. Parcels with sarin gas were abandoned during the rush hours in the crammed wagons of Tokyo's metro by a terrorist group called Aum Shinrikyo. The persons exposed to little quantities of this gas suffered irreparable damages. Twelve people died and more than three thousand resulted affected, most of them still suffering posterior effects that include cerebral damage, respiratory difficulty and depression [1].

2. Chemical agents

A chemical agent is a substance which is intended for use in military operations to kill, seriously injure or incapacitate people because of its physiological effects. The nerve agents are the most toxic of the known chemical warfare agents. They were developed just before and during World War II and are related chemically to the organophosphorus insecticides. The principle agents in this group are:

- GA - tabun
- GB - sarin
- GD - soman
- GF - cyclosarin
- VX - methylphosphonothioic acid

The "G" agents tend to be non-persistent whereas the "V" agents are persistent. They are chemically similar to organophosphate pesticides and exert their biological effects by inhibiting acetylcholinesterase enzymes G-type agents are clear, colorless, and tasteless liquids that are miscible in water and most organic solvents. GB is odorless and is the most volatile nerve agent. At room temperature GB is a comparatively volatile liquid and therefore non-persistent. GB and VX doses which are potentially life-threatening may be only slightly larger than those producing least effects. Death usually occurs within 15 minutes after absorption of a fatal VX dosage.

3. Sensors fabrication

The gas sensors that we employed in our experiments were fabricated over alumina substrates, which included a platinum heater element on the back-side, used for adjusting the sensor operating temperature to the desired value, and gold electrodes on the front side, used to measure the electrical resistance of the sensing films between the electrodes.

Films fabrication consisted in the deposition, at first, of a thick layer of MWCNTs, that was subsequently coated with a thin layer of WO_3 nanoparticles.

The drop coating method was employed to deposit the MWCNT over the sensors substrates. Previously, a uniform functionalization with oxygen plasma was applied to the MWCNTs in order to graft functional groups at their surface and to improve their dispersion and surface reactivity [2]. This activation step was performed at 0.1 Torr, using a power of 30 W and a processing time of 5 minutes, and as a result of this treatment 14 % of atomic oxygen was attached to the nanotubes walls.

In the second step, a layer of WO_3 nanoparticles was deposited over the MWCNTs one by using an advanced

gas deposition unit (Ultra Fine Particle Equipment, ULVAC Ltd., Japan) [3]. Adjusting properly the deposition time, we just a few WO_3 nanoparticles deposited over the carbon nanotube films (Figure 1). The WO_3 showed the tendency to agglomerate over the MWCNTs walls. The deposition time was however not enough to form a homogeneous layer of WO_3 over the MWCNTs, which explains the apparently empty spaces between the WO_3 nanoparticles.

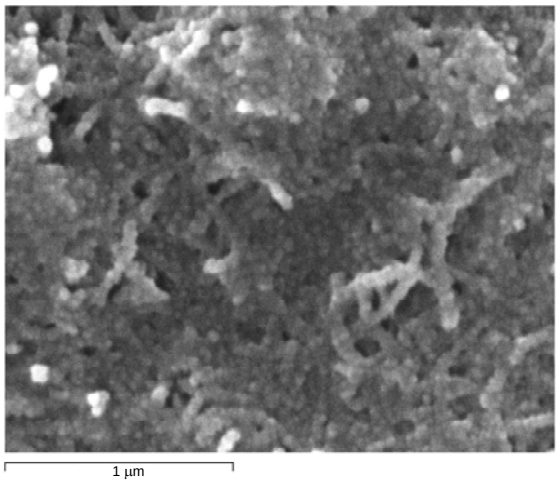

Fig.1. SEM image of the sensors sensitive layer

4. Results of DMMP detection

The ability of the fabricated gas sensors to detect nerve agents was investigated under strictly protected conditions. For performing the measurements, DMMP (precursor of sarin gas) was introduced in the liquid phase in sealed vials. Vapours of DMMP were introduced into the test chamber, where the gas sensors were kept, by means of a headspace sampler (HP-7694), setting the following parameters:

- Oven temperature: 70 ºC
- Loop temperature: 80 ºC
- Transmission line temperature: 90 ºC.

In order to avoid undesired dangerous situations, the sensors were operated at low temperatures during the measurements of DMMP vapour. Concretely, three operating temperatures were tested: the ambient one, 150 and 250 ºC.

The injection time of DMMP into the test chamber was set to 10 minutes, and then synthetic dry air was passes during 1 hour through the chamber for purging purposes. This process was successively repeated for 3 times.

The results obtained showed that, even when operated at room temperature, the sensors were able to detect the presence of the DMMP vapour (Figure 2). But at this low operating, they were not able to desorb the adsorbed DMMP molecules. The same characteristics were obtained when the sensors were operated at 150 ºC.

Nevertheless, when the operating temperature of sensors was raised to 250 ºC (Figure 3), they show the tendency to completely eliminate the adsorbed DMMP vapour, should the purging time be slightly increased.

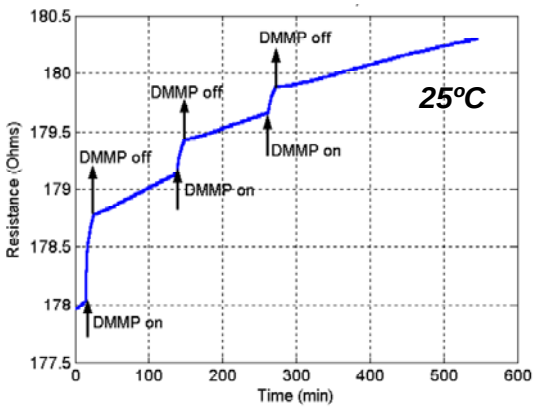

Fig.2. DMMP detection with sensors operated at room temperature

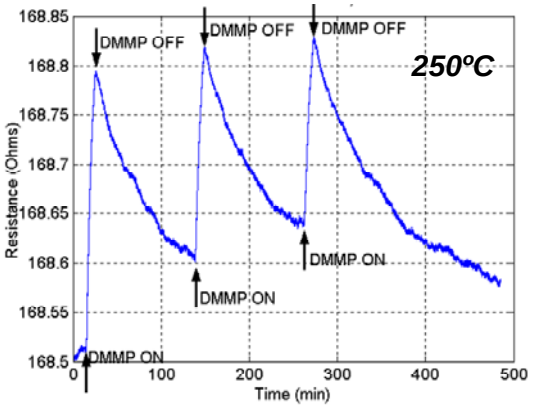

Fig.3. DMMP detection with sensors operated at 150 ºC

5. Conclusions

We show the possibility to detect the precursor of a dangerous warfare agent with small, inexpensive and reliable gas sensors operated at low temperatures. The sensitive materials of the gas sensors were based on superposed layers of multi wall carbon nanotubes (MWCNT) and WO_3.

References

[1] T. Okumura et al., “The Tokyo subway sarin attack—lessons learned”, *Toxicology and Applied Pharmacology*, vol. 207, iss. 2, supplement 1, pp. 471-476, 1 September 2005.

[2] H. Bubert et al., “Characterization of the uppermost layer of plasma-treated carbon nanotubes”, *Diamond and Related Materials*, vol. 12, iss. 3-7, pp. 811-815, 2003.

[3] A. Hoel et al., “Nanomaterials for environmental applications: novel WO3-based gas sensors made by advanced gas deposition”, *Current Applied Physics*, vol. 4, iss. 5, pp. 547-553, 2004.

Guided modes in porous silicon multilayer waveguide structures

E. Xifré Pérez, L.F. Marsal, J. Ferré-Borrull, and J. Pallarès

Departament d'Enginyeria Electrònica, Elèctrica i Automàtica, ETSE, Campus Sescelades, Universitat Rovira i Virgili, Avda. Països Catalans 26, 43007 Tarragona, Spain.

Abstract

We propose a waveguide structure based on porous silicon where the light confinement is not due to the usual total reflection effect but to the use of photonic crystals (PC) as confining walls. These PC are omnidirectional mirrors, that consist of the periodic repetition of two porous silicon layers with different refractive index and thickness. They reflect the radiation for all angles of incidence within a frequency range called the Omnidirectional Band Gap. The photonic crystals formalism has been followed to investigate the properties of the omnidirectional mirror for multimode waveguiding: the number of modes within the band gap and their field spatial distribution.

1. Introduction

One-dimensional photonic crystals are dielectric multilayers that consist of the periodic repetition of two layers with different refractive index and different thickness. They are characterized by the existence of a photonic band gap (BG), a range of frequencies where the light can not propagate inside the structure. These photonic crystals have different applications such as filters [1], microcavities [2], etc. One of these applications are omnidirectional mirrors (OM), where the BG exists for any angle of incidence, the so-called omnidirectional band gap (OBG).

Although different dielectric materials have been used for the fabrication of OM [3], we will focus our attention on OM made of porous silicon [4]. The fabrication technique of this material permits the selection of the refractive index and the thickness of the layers as is explained in [5]. Furthermore, this technology is compatible with existing silicon technology [5].

In this paper, we study a waveguide structure based on porous silicon OM, where the light confinement is not due to the usual total reflection effect but to the use of these photonic crystals as confining walls [6]. In this paper we investigate the necessary conditions for the existence of modes guided by the omnidirectional band gap effect.

2. Structure

The structure of the porous silicon waveguide proposed is presented in Fig. 1. It consists of a core layer inserted in between two symmetric OM. The period of the OM is defined as $\Lambda=d_L+d_H$ and N is the number of periods. The refractive index of the cover medium is n_C and the one of the substrate is n_S. In the studied structure both media are air ($n_C=n_S=1$).

The refractive indices chosen for the OM are $n_H=2.5$ and $n_L=1.5$ [4]. The refractive index of the core layer (n_0) could be any refractive index obtainable with the porous silicon formation technique. In order to choose n_0, the OBG is examined, which is calculated using the transfer matrix method [7], and restricting our discussion to TE modes. For the selected values of n_H and n_L, the OBG exists for $n_0 \le n_L$. When n_0 increases, the width of the OBG decreases but the range of wavectors (possible modes) increases. For a waveguide structure it is interesting to have the widest possible range of wavevectors (β) while maintaining the existence of the OBG. For this reason, $n_0 = n_L = 1.5$ is chosen

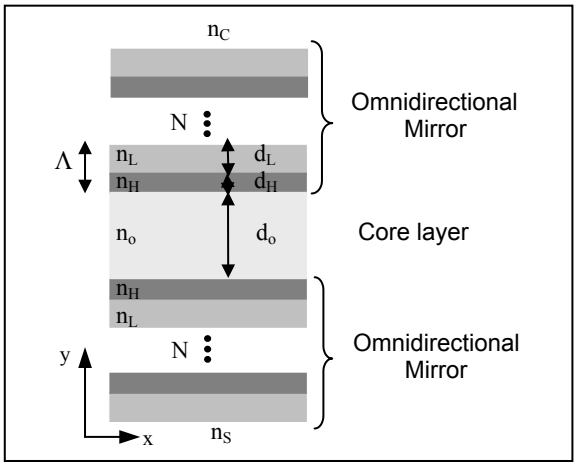

Fig.1. Diagram of the porous silicon multilayer proposed. The refractive index and the thickness of layer i are depicted as n_i and d_i respectively.

For every set of refractive indices n_H, n_L and n_0, there is a value of d_H/Λ (thickness of the high-index layer to the OM period ratio) that maximizes the relative width of the OBG. For the selected refractive indices, this maximum is obtained with $d_H/\Lambda=0.45$. We will choose this value for the OM layer thickness.

3. Modes of the structure

The modal analysis of the waveguide structure has been carried out with the transfer matrix method applied to planar multilayer optical waveguides [8]. The values of β that satisfy the modal condition [eq. 26 in 8] have been calculated and the different types of modes in the multilayer structure are discussed depending on their position in the projected band structure (PBS) of the multilayer. The PBS is obtained using the transfer matrix method [7]. Fig. 2 shows the PBS for $n_H=2.5$, $n_L=n_0=1.5$ and $d_H/\Lambda=0.45$. The light gray regions represent the allowed states and the white region represents the band gap of the OM. The diagonal lines are the 'light lines'. Only the states above the light line for n_0 and within the band gap of the OM are allowed to propagate in the core. The OBG is depicted as the dark gray region.

For this discussion the core thickness $d_0/\Lambda=5$ has been chosen and the frequency anlayzed is $w(\Lambda/2\pi c)=0.285$, that belongs to the OBG. At this frequency and for this core thickness there are seven different β that satisfy the modal condition. The position of these modes in the PBS is shown in Fig. 2 where the plot of the field profile of the most representative is given in the insets. The two modes with the lowest β lie above the light line for either bounding medium $n_S= n_C=1$ but inside the OBG. These are radiation modes [8] since, although they are confined within the core because of the photonic crystal effect of the OM, they can radiate in the cover or substrate, as it can be seen in the inset. The next three modes, $\beta(\Lambda/2\pi)=0.3039$, 0.3740, 0.4139, lie below the light line of the bounding medium and above that of the core. The insets show that the field is confined within the core and is evanescent in the bounding medium. Furthermore, a fundamental mode and successive harmonics can be recognized. Finally, the modes below the light line of the core show an evanescent field in the bounding medium and in the low-index material. Even though these modes are confined in the multilayer structure, they cannot be considered as guided modes by the effect of the OM. Although this study has been done for $d_0/\Lambda=5$, the behavior of the modes is the same for any core thickness.

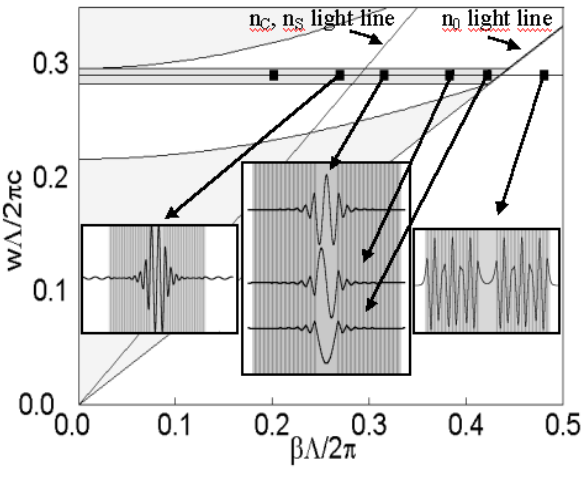

Fig. 2. PBS of the studied structure. The points indicate all the possible modes for $w\cdot(\Lambda/2\pi c)=0.285$, and the insets show the field profile for some of them, superposed on the multilayer structure. The seven modes correspond to $\beta(\Lambda/2\pi)=$ 0.1824, 0.2600, 0.3039, 0.3740, 0.4139, 0.4715, 0.4716.

4. Conclusions

A porous silicon multilayer structure consisting of a core layer inserted in between two symmetric OM has been studied for waveguide applications. The omnidirectional mirror chosen for the structure is the one with the widest OBG obtainable for porous silicon and the core layer refractive index is the low refractive index of the OM. The modes of the structure have been calculated and analyzed depending on their position in the PBS. We have demonstrate that the modes guided in the core layer are the ones with $n_C,n_S<\beta<n_0$.

Acknowledgements. This work was supported by the Spanish Ministry of Education and Science (MEC) under grant number TEC 2005-02038. J.F.B. acknowledges the Ramon y Cajal fellowship from the Spanish Ministerio de Ciencia y Tecnología.

References

[1] E. Xifré Pérez, J. Pallarès, J. Ferré-Borrull, T. Trifonov, and L.F. Marsal, "Low refractive index porous silicon multilayer with a high reflection band", pss(c), (accepted).
[2] M. Ghulinyan, C.J. Otón, Z. Gaburro, P. Bettotti, and L. Pavesi, "Porous silicon free-standing coupled microcavities", Appl. Phys. Lett., 82, 1550 (2003)
[3] Y. Fink, J.N. Winn, S. Fan, C. Chen, J. Michel, J.D. Joannopoulos, and E.L. Thomas, "A dielectric omnidirectional reflector", Science, 282, 1679 (1998).
[4] E. Xifré-Pérez, L.F. Marsal, J. Pallarès, and J. Ferré-Borrull, "Porous silicon mirrors with enlarged omnidirectional band-gap", J. Appl. Phys., 97, 064503 (2005).
[5] A.G. Cullis, L.T. Canham and P.D.J. Calcott, "The structural and luminescence properties of porous silicon", J. Appl. Phys., 82, 909 (1997).
[6] J.S. I, Y. Park, and H. Jeon, "Optimal design for one-dimensional photonic crystal waveguide", J. of Lightwave Technol., 22, 509 (2004).
[7] P. Yeh, Optical Waves in Layered Media, Wiley, New York, 1988, p.102.
[8] J. Chilwell, and I. Hodgkinson, "Thin-films field-transfer matrix theory of planar multilayer waveguides and reflection from prism-loaded waveguides", J. Opt. Soc. Am. A, 1, 742 (1984).

Miniaturized benzene preconcentrator for air quality monitoring

F.Blanco[1*], P.Ivanov[2], M.Vinaixa[1], X. Vilanova[1], I.Gracia[2], C. Cané[2], X.Correig[1]

[1] DEEEA, Universitat Rovira i Virgili Tarragona, Spain
[2] Gas Sensors Group, Centre Nacional de Microelectrònica, CNM-CSIC, Bellaterra, Spain

*Fernando Blanco, Departament d'Enginyeria Electrònica, Elèctrica i Automàtica, Universitat Rovira i Virgili Avinguda dels Països Catalans, 26 Campus Sescelades, 43007 TARRAGONA (Spain)Tel.: +34 977 558 764, Fax +34 977 559 605 e-mail: fernando.blanco@urv.cat

Abstract: In this paper, we present a miniaturized benzene preconcentrator. The device is based on an adsorbent layer (Carbopack X) placed on an alumina substrate. Concentration factors up to 300 has been obtained allowing a significant improvement of the usual detection margins of a gas sensor.

Keywords: preconcentrator, benzene detection, activated carbon layers.

INTRODUCTION

Nowadays, the monitoring of volatile organic compounds (VOCs), that can cause a range of adverse health effects has received a great deal of attention. Benzene, in particular, has been shown to be an important carcinogen in studies of human health. It is present in outdoor and indoor environments. As part of the Air Quality Framework Directive of the European Union (Directive 96/62/EC), the "Daughter" Directive (Directive 2000/69/EC) for benzene sets the annual mean limit value at 5 μg m^{-3}, standardised to 293 K and 101.3 kPa [1]. The benzene is included in the known chemical group of aromatic compounds. For the detection of this type of gases, different techniques mainly based in gas chromatography, has been developed. They used to incorporate preconcentrator systems with the aim to detect low VOCs concentrations.

Recent studies have shown that adsorption of benzene can be significantly improved by using graphitized carbon such as Carbograph, Carboxen, Carbopack B and Carbopack X.[2].

PROCESS OF FABRICATION

Selecting the adsorbent

There is a wide range of adsorbent materials to be used in the field of thermal desorption. Often, choosing the right one is a difficult task.

Differences between adsorbents are based on their capability to efficiently retain and release an analyte. In the strong adsorbents analytes are retained to the point that they are not efficiently released during the desorption process and a portion of them can be observed when a subsequent desorption is carried out. In the case of “irreversible adsorption” the analyte can not be released from the adsorbent and is not observed in the second desorption.

Recoveries of 80% or greater are typically considered acceptable in most thermal desorption methods. When recoveries are between 21 and 79 % a significant amount of the analyte is recovered from the adsorbent, but warns the user that break through occurred or that the analyte is too strongly retained. A recovery less than 20 % is simply not suitable for any sampling application [3].

In the miniaturized preconcentrator presented in this work the adsorbent selected is Carbopack X. It has a surface area 240 m^2/gr and excellent affinity to benzene.

Fabrication of the preconcentrator

Using screen-printing technique, a layer of TEMPFLEX 5145 were deposited on alumina substrates. TEMPFLEX is a non-corrosive adhesive, which offers excellent adhesion to ceramics and retains its characteristics over a wide temperature range, resisting long term exposure at 300°C. After this, 2.4 mg de Carbopack X is spread over the surface in order to create the absorbent layer with area of ≈16 mm^2. The structure of the fabricated concentrator is shown on Fig 1.

In order to functionalize the Carbopack X, an annealing in nitrogen atmosphere at 300 ºC for 5 hours was performed.

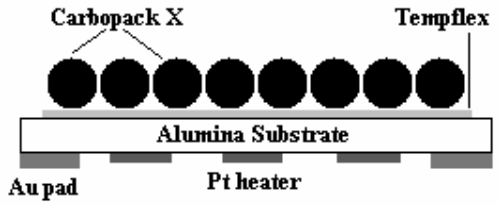

Fig. 1Schematic diagram of the fabricated preconcentrator.

RESULTS AND DISCUSSION

Structural studies

The morphology and composition of the screen-printed sensing layers was studied by scanning electron microscopy (SEM) and energy-dispersive X-ray spectroscopy (EDX). Samples were previously coated with a thin (20 nm) gold layer to avoid charging effects. Specimens were observed at accelerating voltages 20 kV using a JSM 6400 field emission scanning electron microscope.

The total thickness measured for the absorbent layer was 400 μm being the particle size around 320 μm. The SEM analysis showed that the absorbent layer obtained is highly porous.

In figure 2 we present the SEM micrograph of a single carbon particle. It could be clearly observed

that the fabrication process is not affecting the porosity of the absorbent layer.

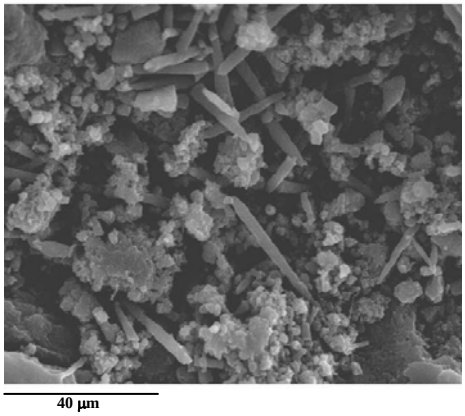

Fig. 2 SEM micrograph of the carbon structure after fabrication.

Measurement system

In order to obtain the concentration factor of the fabricated preconcentrators a GC/MS Shimadzu QP-5000 equipment has been used. A 6 ways valve has been incorporated in its entrance to be able to make the experiments. A schematic view of the measurement system could be observed on Fig. 3.

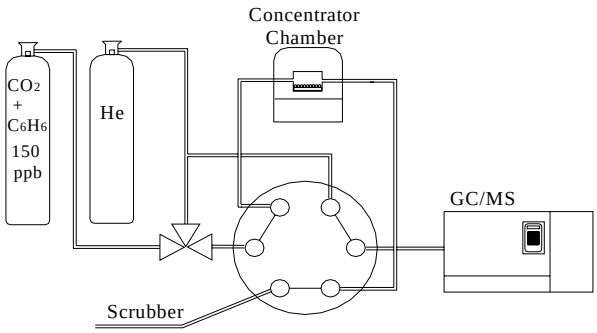

Fig. 3 Measurement system.

Adsorption measurements

The measurement process is composed of two steps. First, a monitoring of the bottle concentration was performed by means of five consecutive measurements called blanks.

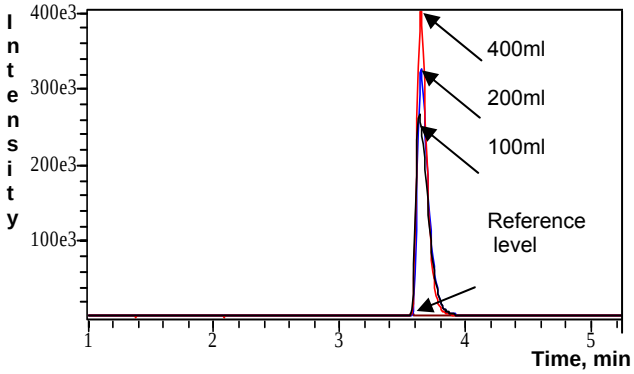

Fig. 4 Typical chromatogram of blank/desorption.

The values obtained allow us to define the average benzene concentration in the calibrated bottle (reference level). In the next step, a series of three adsorption/desorption processes, using the miniaturized preconcentrator, were made. On Fig. 4 a typical chromatogram of desorption could be observed. The small peak corresponds to the reference level obtained while the bottle concentration was measured.

The concentration factor was calculated by comparing the average peak values obtained from the blank and desorption. In the present case, the average concentration factor (based on 5 preconcentrators) reached 300 times. Results obtained from the measurements of the preconcentrators at different airflow are presented in Table 1.

Table 1 Measurement results.

Airflow x 10 mins	***Concentration Factor (CF)***	***CF x area***
100 ml	***245***	***16 times x mm^2***
200 ml	***265***	***18 times x mm^2***
400 ml	***300***	***20 times x mm^2***

Gas sensor measurements

Additional measurements were performed using pure and doped metal oxide gas sensors [5]. In figure 5 a sensor response to 500 ppb of benzene is presented. Firstly (fig 5a), when no preconcentrator is used the signal output of the sensor is very low, whereas when the preconcentrator is used (fig 5b) a sharp response is obtained.

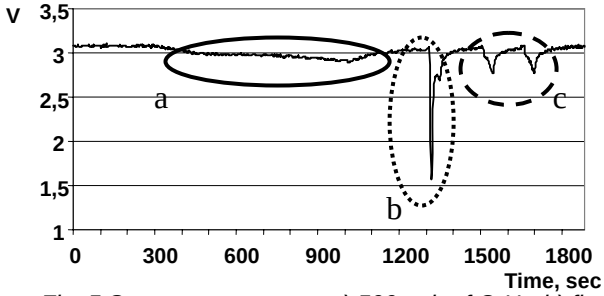

Fig. 5 Sensor response to: a) 500 ppb of C_6H_6; b) first desorption; c) residual desorption

4. CONCLUSIONS

The results obtained with the miniaturized preconcentrators showed high repeatability and preconcentration factors up to 300 times. The small size of the manufactured devices enables their incorporation in an integrated GC-gas sensor system.

REFERENCES

[1] N. Martin et al, *Atmospheric Environment* 37 (2003) pp. 871-879

[2] B. Strandberga et al, *Atmospheric Environment,* (2005) 39 pp. 4101- 4110

[3] J. Brown, SUPELCO Technical report (2001)

[4] R. Manginell, *Sandia Natoional Laboratories Report* (2000) P820C

[5] E. Llobet et al, *Sensors and Actuators B* 96 (2003) pp. 94–10

Analysis of optical systems based on vortical scattering parameters

A.Lázaro[1], A.Belmonte[2]

[1]Dept. of Electronics and Automatic Engineering, Rovira Virgili University, 43007 Tarragona, Spain
Phone: +34-977-558668; fax: +34-977-55905, antonioramon.lazaro@urv.net
[2]Dept. of Signal Theory and Communications, Tech. Univ. of Catalonia, 08034 Barcelona, Spain

Abstract

The application of scattering matrix theory in optics has usually been limited to multilayer propagation of plane waves but the analysis of spatial diffraction, the most characteristic effect of any optical element, has had to be considered through techniques much less competent. This paper describes the use of a generalized modal scattering matrix theory as a fast, efficient approach to the analysis of optical systems. In contrast with other methods, the new technique uses a type of optical vortices, called Bessel beams. This rigorous modelling technique has interest in areas of optics as diverse as optical communications, spectrometry, integrated optics, and remote sensing systems. The tactic allows solving both multilayered reflections problems and spatial diffraction phenomena using scattering parameters associated with the transmitted and reflected vortical spectrum.

1. Introduction

Optical systems and microwave circuits share many fundamental properties. Both of them describe fields and physics devices in terms of linear differential operators and consider the principle of superposition. Although it is tempting to carry over directly all the techniques that have been developed over the years in electrical circuitry and bring them to bear on problems of analysis and design of optics, optical systems have inherent properties which make them essentially different from microwave circuits. For all intents and purposes, the application of scattering theory in optics has usually been limited to multilayer propagation of plane waves, but the analysis of spatial diffraction, the most characteristic effect of any optical element, has had to be considered through techniques much less competent. One of the most used approaches, the angular spectrum propagation method, analyzes the propagation of optical perturbations through systems consisting of optical elements, apertures, and free space regions using two-dimensional fast Fourier transforms. By using Fourier techniques, the incident beams are decomposed in plane waves that propagate through the optical system. However, although this method requires a larger number of plane waves to represent typical optical perturbances, it deals very poorly with optical interferometric systems (e.g. Fabry-Perot and Fizeau filters), or systems where multiple reflections need to be accurately considered to describe correctly their behavior. Consequently, methods other than those based on angular spectra are required to solve this set of problems.

We aim to address these difficulties. This work defines the use of a novel, generalized modal scattering matrix as a fast, efficient approach to the analysis of optical systems. In contrast with other methods, the new technique uses Bessel beams [1], a type of optical vortices, as the basic modal expansion characterizing optical signals.

$$U(\rho,\phi) = \sum_{m=-M}^{M} \sum_{n=0}^{N} a_{mn} J_m(\nu_{mn}\rho)\exp(-jm\phi) \qquad (1)$$

where J_m is the *m-th* order Bessel function of the first kind and ν_{mn} the spatial frequencies of the harmonic functions describing the complex amplitude U. The spatial frequencies ν_{mn} distinguish any of the optical modes used to describe the complex amplitude U. The angles θ_n of the wavevector are related to the spatial frequencies ν_n by $sin\theta_n=\lambda\nu_n$, where λ is the wavelength of light.

Bessel beams are free-space, exact solutions of the wave equation that are not subject to transverse spreading (diffraction). These nonsingular solutions, like plane waves, have finite energy density rather than finite energy. They have sharply defined intensity distributions as small as several wavelengths in every transverse plane, independent of propagation distance [1]. This feature is most relevant for the purposes of optical signal modal decomposition. In the next sections, we define the generalized scattering parameters and typical systems are solved using this technique in realistic environments.

2. Generealized Scattering Matrix

This work extends the S matrix theory based on the angular spectrum for propagating waves by using Bessel beams, a type of optical vortices, as the basic modal expansion characterizing optical signals. The transverse electric and magnetic field can be written as the sum of reflected and transmitted waves or modes, with

amplitudes E^i_l and E^r_l. and longitudinal component of the wave vector $k_{z,l}(\nu_l)$ for the l-mode, and $\nu_l=\nu_{mn}$ is the radius of the circular masses associated to the Bessel modes spectra. These waves are analogous to the forward and reflected travelling voltage on a transmission line. We can define normalized waves incident and reflected waves at port k for the mode m as:

$$a_{k,l} = \frac{E^i_l}{\sqrt{|\mathrm{Re}\, Z_{k,l}|}}; b_{k,l} = \frac{E^r_l}{\sqrt{|\mathrm{Re}\, Z_{k,l}|}} \quad (2)$$

Here, $Z_{k,l}$ is the reference impedance at port k for the mode l. This impedance is usually chosen equal to the medium impedance for this mode, Z_l. For the arbitrary diffractive optical device shown in Fig.1, each incident Bessel beam with order l at port i, $a_{i,l}$, produces reflected Bessel modes at port i, $b_{i,l}$ and transmitted Bessel modes at port j, $b_{j,l}$. As the device is diffractive, each input Bessel beam generates a complete set of output modes. The generalized scattering parameters can be defined at input port i with input mode m and output port j and mode n:

$$S_{ji,mn} = \left.\frac{b_{j,n}}{a_{i,m}}\right|_{a_{k,v}=0, k\neq i, v\neq m} \quad (3)$$

Arbitrary optical systems can be analysed using this generalized scattering parameters. Each optical subsystem is connected to other subsystems in the same way as microwave circuits. With this modal method, reflection between subsystems are taken in count with the S-parameter formulism. This formalism allows to consider diffractive optics by defining non-diagonal S-matrix. The computationally expensive 2-D convolution of plane waves in classical beam propagation methods is here a simple product of full modal S-matrix. Non-diffractive optical elements have diagonal S-matrix, as it has the non-diffractive propagation of our Bessel beams. To obtain the S parameter of an optical system from the S parameters of the composed optical subsystem the same analysis techniques than in microwave networks can be used.

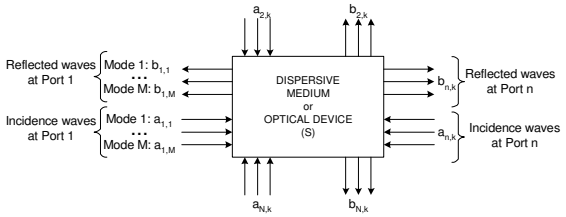

Fig.1. Outgoing and incoming for each wave mode in an optical network.

3. Simulated results

The next figures show the output of common optical subsystems such as etalons, lenses with aberrations, Fizeau devices and gratings when are illuminated with arbitrary illuminations (e.g. gaussian beams). In the case of grating, the S matrix it is calculated using RCWA technique previously developed in the literature for plane waves. This fact demonstrates the possibility to integrate results obtained with other full-wave techniques. Note that diffraction effects and interference are take account automatically by the technique implemented in a software called VBS.

As conclusion, it has been remarked that Bessel beams are a kind of optical vortices. The study of optical vortices is becoming extremely important from the viewpoint of both fundamental and applied optics. The unique nature of an optical vortix is likely to lead to new applications in many areas of optical science and engineering. Using these special solutions of the wave equation for this first time as an alternative approach to Fourier optics, our technique also preludes the potential of optical vortices in the area of design and analysis of complex systems in optics.

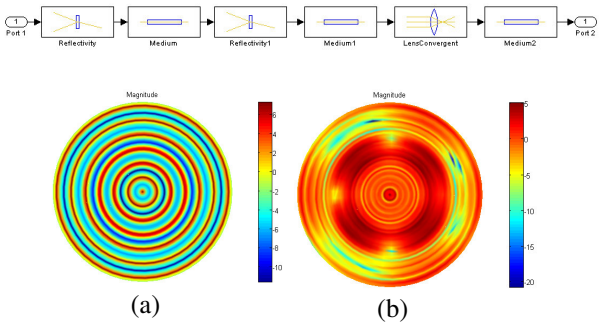

Fig.2. (a) Fringes at the output of an etalon with an optical formation system (lens). Etalon's reflectivity, R=0.9, Etalon's gap 50 mm, Input Beam is a Gaussian Beam, Width 20 cm. (b) Effect of astigmatism on Etalon's surface.

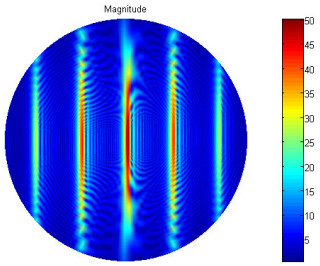

Fig.3. Magnitude of the electric field at the output of Fizeau device (wedge angle, 47 μrad) illuminated with a gaussian beam.

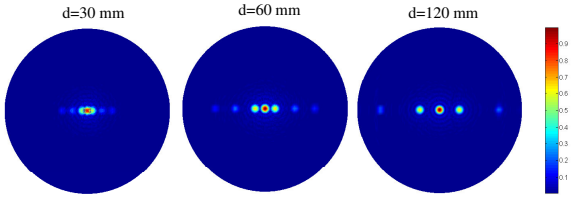

Fig.4. Gaussian beam (2 mm $1/e^2$ width) diffracted by a grating (Period=10λ, fill-factor=0.5) as a function of grating distance d.

Reference

[1] J. Durnin, "Exact solutions for nondiffracting beams. I. The scalar theory," J. Opt. Soc. Am. A, Vol.4, 651-654, 1986.

A Compact Quantum Model of Nanoscale Double-Gate MOSFET for RF and Noise Simulations

A.Lázaro, B.Nae , O.Moldovan, B.Iñíguez

Dept. of Electronics, Electrics, and Automatic Engineering, Universitat Rovira i Virgili, 43007 Tarragona, Spain,
Phone: +34-977-558668; fax: +34-977-55905. Email: antonioramon.lazaro@urv.net

Abstract

In this paper, we present a new analytical model for RF and microwave noise model of nanoscale double-gate MOSFET. The model is based on a compact model for charge quantisation within the channel and it includes overshoot velocity effects. RF and noise performances are calculated using active transmission line method. A comparison between classical and quantum charge control, and between drift-diffusion and hydrodynamic models is done.

1. Introduction

Double-gate (DG) MOSFET transistors are considered to be a very attractive option to improve the performance of CMOS devices and overcome some of the difficulties encountered in the downscaling of MOSFETs into the sub-50 nanometer gate length regime. Due to scaling, the silicon thickness is ultra-thin and quantum confinement must be included in the models[1]. Then, a self consistent solution of Schrödinger-Poisson equations is needed. We obtain a new compact charge control model including quantum effects whose explicit formulation is similar to classical charge control. Velocity overshoot is included in the model using a one-dimensional energy-balance model [1]. In contrast with model presented in [1], we include the effect of saturation region and the channel modulation length effect. The low-field mobility data uses a model that takes into account the mobility degradation due to quantum effects.

The DC model is extended to RF/microwave frequency range using the active transmission line approach [2-3]. Diffusion and shot noise sources are included in the active line in order to study noise behavior of these transistors. Needless to say that carrier temperature has a great influence in high frequency noise behavior. Whereas in the drift-diffusion models the carrier temperature is considered using empirical relationships with electric field, in the model presented here, the carrier temperature along the channel is obtained from the energy-balance model. In contrast with previously models for DG MOSFETs [2-3], this paper presents for the first time a compact model for RF/noise applications including quantum effects and hydrodynamic transport. A comparison between drift-diffusion model and non-stationary model will be presented.

2. Model and results

By integrating the Poisson equation between the center and the surface of the film we get obtain the electric field as function of the potential difference between surface and center potential, $\phi_S - \phi_0$ [3]. Defining the average penetration of the inversion-charge distribution y_I into the silicon [4] we obtain:

$$\phi_S - \phi_0 = y_I Q / 2\varepsilon_{si} + Q_{Dep} / 8C_{Si} \qquad (1)$$

where $C_{Si}=\varepsilon_{Si}/t_{Si}$ represents the silicon film capacitance. Note that, for weak inversion, the term $y_I Q << Q_{Dep}/8C_{si}$ in (1) may be simplified [3]. In order to calculate the charge densities from an explicit expression of the applied bias, we use the following equation:

$$\frac{Q}{2C_{ox}} = -\frac{2C_{ox}\beta^2}{Q_{Dep}} + \sqrt{\left(\frac{2C_{ox}\beta^2}{Q_{Dep}}\right)^2 + 4\beta^2 \log^2\left[1 + e^{\frac{V_{GS}-V_{th}-V}{2\beta}}\right]} \qquad (2)$$

where $\beta=kT/q$ and V_{th} is the threshold voltage.

Due to the confinement of electron motion normal to the Si–SiO interface, the conduction band within the transistor channel is split in several subbands, each of which is associated with the corresponding energy eigenvalue. A first approximation for the eigenvalues is given using square potential well. Using this approximation a good estimation of V_{th} and a simple charge model can be obtained from [1]. Nevertheless the quantum compact model [1] doesn't agree with self consistent solution of Schrödinger-Poisson numerical simulations (using SCHRED [5]) in the strong inversion region, but the agreement is better for low gate bias. These discrepancies arise from the infinite potential well approximation and the uniform charge distribution in the well assumed equal to mean value used in the eigenvalue calculation, in spite of a second order correction performed later to improve the first eigenvalue estimation. For higher gate bias voltage the eigenfunctions differs from the eigenfunctions in a infinite potential well.

A simple relationship between inversion centroid and inversion charge obtained fitting numerical simulation results is given in [4]. However, the inversion centroid is a function of the inversion charge Q. Using this analytical expression a correction for oxide capacitance given can be found:

$$C_{ox}^{*} = C_{ox} / \left(1 + C_{ox} y_I / \varepsilon_{si}\right) \qquad (3)$$

A first iteration of the charge using the compact model [1] is used to calculate the corrected oxide capacitance, and then, using (2) we obtain the inversion

charge replacing C_{ox} by C_{ox}^{*}. A comparison of this model with numerical classical and quantum simulations is performed using SCHRED [5] with good agreement in the two cases.

In extremely short channel DG MOSFET the channel is quasi-ballistic, thus an important overshoot velocity is expected. Using a simplified energy-balance model [1], the electron mobility is a function of the electron temperature related to the average energy of the carriers. The electron temperature T_e is governed by the following equation:

$$\frac{dT_e}{dx}+\frac{T_e-T_0}{\lambda_w}=-\frac{q}{2k}E_x(x) \qquad (4)$$

where the energy-relaxation length is defined as $\lambda_w=2v_{sat}\tau_w$, τ_w being the energy relaxation time, and v_{sat} the saturation velocity. Using the charge control models previously presented and the velocity-field relationship for the stationary case, the drain current in the linear channel region can be obtained [1]:

$$I_{DS}=\frac{W\int_0^{V_{Dsat}}\mu_{n0}Q(V)dV}{\int_0^{L_e}\left(1+\alpha(T_e(x)-T_0)\right)dx} \qquad (5)$$

where $\alpha=2k\mu_{n0}/q\lambda_w v_{sat}$. In the quantum case, using effective mobility, the charge integral in (5) can be evaluated numerically.

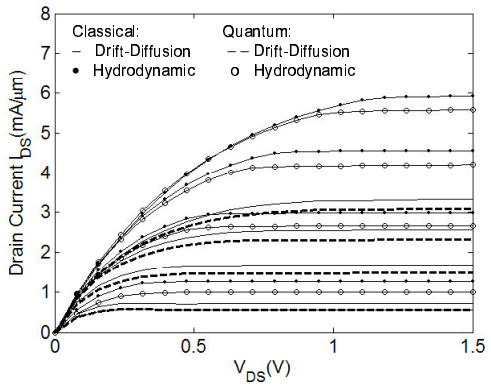

Fig.1. A comparison of drain current for DG MOSFET (Na=6·1017 cm-3), L=50 nm, t_{si}=5 nm, t_{ox}=1.5 nm for classical charge control (V_{gs}-V_{TH}=0.5, 1, 1.5 and 2 V)

In order to evaluate the integral of the denominator of (5), we need to know the temperature profile along the channel. As a first approximation, in the linear region we can suppose that the lateral field is linear from a small value at the source end to the saturation field at $x=Le$ ($E_x=E_{sat}\cdot x/L_e$).

Then, using the segmentation method or active transmission line analysis, the channel is divided in channel sections or slides, and the S parameters and noise parameters of the device are obtained using the method described in [2]. Some results for DC, transition frequency and intrinsic noise parameters for drift-diffusion and hydrodynamic using classical and quantum compact charge model are presented in fig.1-3.

As a conclusion, the results show important differences in drain current, f_T and noise performances between drift-diffusion and hydrodynamic models for short gate lengths. These differences are due to the velocity overshoot increasing the transconductance, and the hot-carrier effects in the noise temperature.

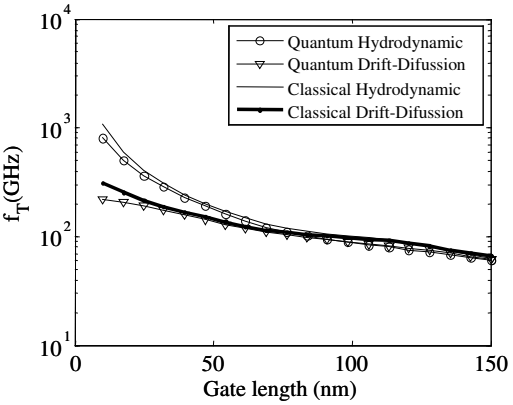

Fig. 2. Simulated cut-off frequency f_T versus gate length for DG MOSFET (Na=6·1017 cm-3, W=10 μm). Vds=1V, V_{gs}-V_{TH}=0.5V.

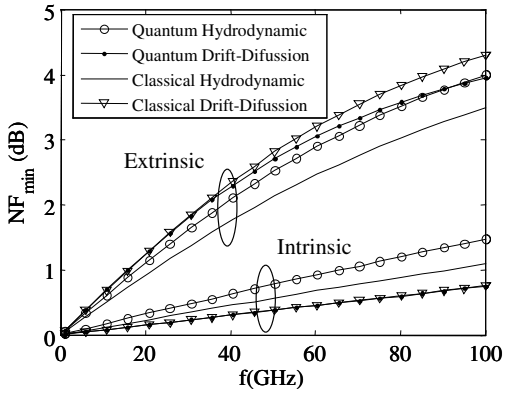

Fig.3. Minimun Noise Figure for DG MOSFET (t_{ox}=1.5nm, L=12.5 nm, t_{si}=0.4L,10 fingers, W=10 μm, V_{gs}-V_{TH}=0.5V, V_{ds}=1V).

Acknowledgements

This work was supported by Project TEC2005-06297/MIC, by the European Commission under Contract 506844 ("SINANO") and Contract 506653 ("EUROSOI").

References

[1] G.Baccarani G, and S.Reggiani. "A Compact Double-Gate MOSFET Model Comprising Quantum-Mechanical and Nonstatic Effects". *IEEE Trans. on Electron Devices*, Vol.46, No.8, pp.1656-1666, 1999.

[2] A.Lázaro A, B.Iñíguez. "RF and Noise Performance of Double Gate and Single Gate SOI. Solid-State Electronics", Vol.50, pp. 826-842, 2006.

[3] B.Iñíguez, A.Lázaro, O.Moldovan,A.Cerdeira, T.A.Fjeldly. "DC to RF Small-Signal Compact DG MOSFET model", Workshop on Compact Modeling, Boston, 2006.

[4] J.A. López-Villanueva, P.Cartujo, F.Gámiz, J.Banqueri, A.J.Palma. "Effects of the Inversión-Layer Centroid on the Performance of Double-Gate MOSFET's". *IEEE Trans. On Electron Devices*, Vol.47, no.1, pp.141-145, 2000.

[5] D.Vasileska, Z.Ren, SCHRED-2.0 Manual. Tempe, AZ: Arizona State Univ.Press, Feb.2000.

RF MEMS Dynamics and Power Handling Characterization Platform Based on Microwave Instrumentation

David Girbau*, Lluís Pradell*, Antonio Lázaro**, N. Otegi***

* Signal Theory and Communication Department, University Politècnica de Catalunya (UPC), Campus Nord UPC – Mòdul D3, 08034 Barcelona – Catalunya, Spain, fax: +34-93-4017232 pradell@tsc.upc.edu ** Electronics, Electrical and Automatics Engineering Department, University Rovira i Virgili, 43007 Tarragona, Spain
*** Electricity and Electronics Department, University of the Basque Country, 48080 Bilbao, Spain

***Abstract* – This paper presents a multidisciplinary characterization platform for RF MEMS measurement, based on microwave instrumentation. The platform has been designed to characterize mechanical parameters –dynamics: actuation and release times, resonance frequency and damping–, of both, MEMS capacitors and switches.**

I. INTRODUCTION

Deep expectations to obtain low-cost, integrated, high-performance devices have been generated by RF MEMS technology. However, still a number of issues are unsolved, not only from the technological point of view and from the design concept, but also from the point of view of device characterization. Mechanical characterization can be done by means of optical techniques [1], but they are limited to unpackaged devices. On the other hand, RF MEMS are multidisciplinary devices and therefore have to be addressed globally, mainly due to the strong connection between mechanical and RF performance. In consequence, device characterization from multiple points of view (mechanical, RF static performance and non-linear behaviour) using microwave measurements, is essential. Indeed, microwave setups to measure dynamics of MEMS switches [2-3] have already been reported. Moreover, measurement of MEMS power handling based on power detection [4-5]. This paper presents a multidisciplinary characterization platform of RF MEMS, based on instrumentation typically available in microwave laboratories, along with several measurement techniques. The platform combines several measurement systems previously reported by the authors [6,7] to characterize mechanical dynamics –actuation time, release time, transfer function– and RF power handling.

II. RF MEMS MECHANICAL DYNAMICS AND RF POWER HANDLING MEASUREMENT TECHNIQUES

For parallel-plate RF MEMS modelled as in Fig.1, a general exciting voltage at the device reference plane containing RF and low frequency waveforms is assumed:

$$V = V_{Bias} + V_{RF} = V_B \cos \omega_B t + V_o \cos \omega_{RF} t \qquad (1)$$

The electrostatic force depends on the squared voltage, given by:

$$V^2 = \frac{V_B^2}{2} + \frac{V_0^2}{2} + \frac{V_B^2}{2}\cos(2\omega_B t) + \frac{V_0^2}{2}\cos(2\omega_{RF} t) + V_B V_0 \left[\cos(\omega_{RF} t + \omega_B t) + \cos(\omega_{RF} t - \omega_B t)\right] \qquad (2)$$

The device RF voltage can be expressed as a superposition of an incident and a reflected wave (3), related through the MEMS reflection coefficient (Γ_{MEMS}):

$$V_{RF}^- = V_{RF}^+ \Gamma_{MEMS} = \left|v_0^+\right| e^{j\phi^+} \left|\Gamma_{MEMS}\right| e^{j\phi_{MEMS}} \qquad (3)$$

being:

$$\left|\Gamma_{MEMS}\right| = \frac{\sqrt{\left(R^2 - Z_0^2 - \left(Z_0 \omega C R\right)^2\right)^2 + \left(2 Z_0 \omega C R^2\right)^2}}{\left(R + Z_0\right)^2 + \left(Z_0 \omega C R\right)^2} \qquad (4)$$

$$\angle\Gamma_{MEMS} = \arctan\left(\frac{-2 Z_0 \omega C R^2}{\left(R^2 - Z_0^2\right) - \left(R \omega C Z_0\right)^2}\right) \qquad (5)$$

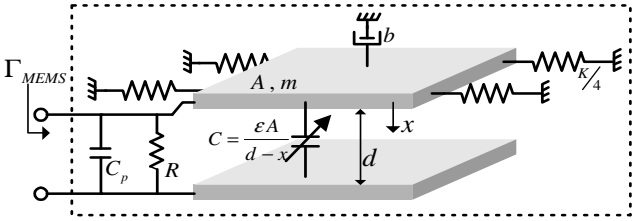

Fig.1. Model of a parallel-plate RF MEMS.

The reflection coefficient is time-dependent due to the bias waveform (see expression (2)). From (3), it follows that the displacement variations –included in the capacity, C– can be obtained from both, the magnitude and the phase of the reflection coefficient, which, in turn, are obtained from the magnitude and phase of the reflected signal at the device. However, [6] demonstrates that phase detection is preferred to magnitude detection.

A. Mechanical dynamics characterization.

By applying the signal defined in (1), the bias signal being in this case a squared wave, the instantaneous phase and magnitude of the RF signal reflected at the capacitor is proportional to the displacement of the mobile membrane, and therefore, information about the actuation and release times is obtained.

Measurement of the mechanical transfer function can be done twofold, always by applying a bias sinusoid: 1/ from the variation of the sidebands which appear as a result of the phase modulation which generates the term $V_B^2 cos(2\omega_B t)/2$ in (2), or 2/ from the excursions of the device reflection coefficient phase (magnitude excursions, as already introduced are much smaller), by sweeping ω_B.

B. RF power handling characterization.

The limitation of parallel-plate MEMS devices to work with high RF powers arises mainly from two phenomena:

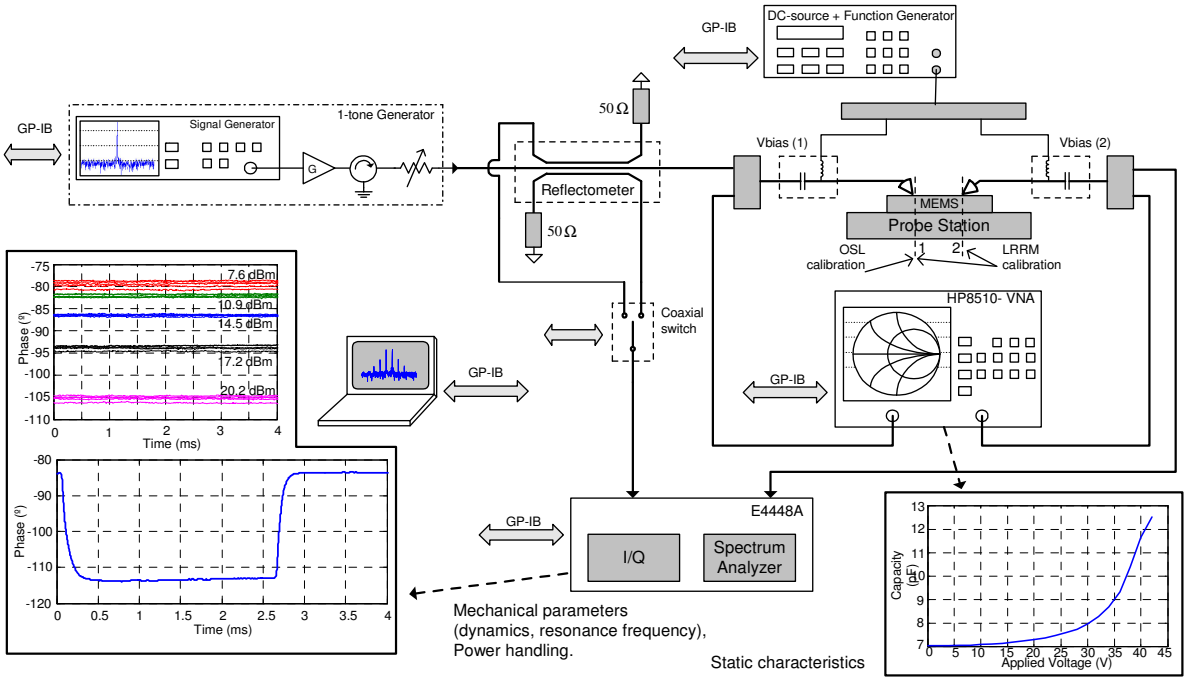

Fig. 2. Diagram of the RF MEMS multidisciplinar measurement platform.

self-actuation due to the voltage at the capacitor (the term $V_0^2/2$ in (2)) and excess current density, whose effect is similar to self-actuation, resulting in a downward buckling of the suspended structures. This effect is characterized by measuring the constant membrane displacement (at constant RF power). The effect due to RF power resulting from both contributions can be obtained by sweeping the RF voltage at the device V_0 (that is, by sweeping the RF power).

III. RF MEMS CHARACTERIZATION PLATFORM

Fig.2 shows the RF MEMS multidisciplinary characterization platform. The MEMS actuation voltage is provided by a DC-source and a function generator (DC voltage or a sinusoidal/square function or an arbitrary waveform can be generated). A 1-tone generator is used, composed by a signal generator, a power amplifier, a circulator and a variable attenuator. In this way, a variable power can be delivered to the device under test (DUT).

A reflectometer is inserted between the signal generator and the MEMS. It is used for sampling the reflected signal at the device. In addition, the RF signal delivered to the MEMS is also sampled. A coaxial switch is used in order to select the two signals.

Measurements are done with an Agilent E4448A Spectrum Analyzer. When used as an I/Q demodulator, phases and magnitudes of these two sampled signals are obtained; in this way an OSL calibration can be done for corrected device reflection coefficient. From this, variations in the device reflection coefficient magnitude and phase can be processed in order to obtain dynamics and power handling effects on the mobile membrane displacement.

Examples on measurement capabilities of MEMS capacitors are shown in Fig.2. Concerning the dynamics measurement, the actuation and release times of a parallel-plate capacitor are shown. The effects of RF power handling in the capacitor are also presented; it can be observed how the membrane deflects with an increasing RF power.

IV. CONCLUSION

A RF MEMS multidisciplinary characterization platform, based on instrumentation typically available in microwave laboratories has been presented. The system demonstrates the capability of characterizing small-power static parameters along with dynamics and RF power handling in RF MEMS devices.

ACKNOWLEDGEMENT

This work has been supported by Spanish Government Project ref. ESP2004-07067-C03-03, MCYT (Ministerio de Ciencia y Tecnología).

REFERENCES

[1] E.Lawrence, K.Speller, "MEMS characterization using laser Doppler vibrometry". Polytec, Applied MEMS.

[2] S.Mellé, F.Flourens, D.Dubuc, K.Grenier, P.Pons, J.L.Muraro, O.Vendier, R.Plana, "Early degradation behaviour in parallel MEMS switches". MEMSWAVE, 4th WorkShop on MEMS for millimeterwave communications, pp.F-33 – F-36. July 2003.

[3] D.Peroulis,S.P.Pacheco,K.Sarabandi,L.P.B.Katehi, "Electromechanical Considerations in Developing Low-Voltage RF MEMS Switches", IEEE Transactions on MTT, vol. 51, nº1, January 2003.

[4] D.Peroulis, S.P.Pacheco, L.P.B.Katehi, "RF MEMS Switches With Enchanced Power-Handling Capabilities", IEEE Transactions on MTT, vol. 52, nº1, January 2004.

[5] B.Pillans, J.Kleber, C.Goldsmith, M.Eberly, "RF Power Handling of Capacitive RF MEMS Devices", 2002 IEEE MTT-S Int. Microwave Symposium Digest, vol. 1, pp. 329-332. June 2002.

[6] D.Girbau, A.Lázaro, L.Pradell, "Characterization of dynamics and power handling of RF MEMS using vector measurement techniques", *IEEE Trans. Microwave Theory and Techniques, Vol. 52, Nº 11, pp. 2627-2633, Nov. 2004.*

[7] D.Girbau, N.Otegi, L.Pradell, A. Lázaro, "Study of intermodulation in RF MEMS capacitors", *IEEE Trans. Microwave Theory and Techniques, Vol.54, Nº3, pp.1120-1130. March, 2006.*

Taking advantage of the time dimension on MS-Sensor profiling approaches: Evaluating Iberian Ham quality using HS-MS and multi-way data analysis

Maria Vinaixa[1], Raúl Calavia[1] , Jesus Brezmes[1], Atanasio Carrasco[2], Xavier Correig[1]
Departament d'Enginyeria Electrònica, Elèctrica i Automàtica, ETSE, Universitat Rovira i Virgili, Avda. Països Catalans, 26, 43007 Tarragona maria.vinaixa@urv.net

1. Introduction

Electronic noses have been used to measure the volatile fingerprint profile of samples. Sample treatment is eliminated or reduced to a minimum, and chemometric techniques are used to extract the information contained in the profile signals. Recent research has shown that the rapid analysis of the global volatile fraction of foods by mass spectrometry without chromatographic separation produces signals (signatures) containing significant information; owing to their immediacy, these nonseparative methods can be used for the classification and prediction of the volatile signatures of the products

In Spain the products derived from Iberian pigs constitute an important economic activity. Much attention has been devoted to the study of dry cured ham in recent years. Volatile compound composition of ham is markedly affected by pig feeding. The feeding pigs receive contributes in a remarkable way to the sensorial characteristics of hams such as flavour, those most appreciated being those coming from pigs fattened with acorn. Thus this is affecting then to quality of hams in general. Techniques used until now to evaluate the quality of hams in general are time consuming, have a low throughput and are expensive. This fact brings the necessity of a near-real time method to assess the quality of hams in general. Such method would help regulatory authorities and even final consumers to avoid frauds in the Iberian ham commercialization. MS-Sensors acting as an electronic nose could be a good candidate as technique for assessing the quality of hams. Common pattern recognitions algorithms applied on MS-Sensor data make use of the averaged mass spectra along the detected peak. For a given measurement, the resulting mass spectrum gives a fingerprint that is characteristic of the volatile compounds present in the headspace of the hams. Considering this average mass spectrum sometimes can lead to losing useful of temporal information. Even chromatographic resolution is avoid along the time axis, some sort of diffusion is observed on the isothermal peak. This leads us to consider the possibility to compute this extra-information by considering the 3 way nature of the data by means of the use of 3-way algorithms. Multi-way methods are particularly useful for the analysis of batch process data and analytical data where a response is being measured as a function of two or more parameters. Examples include many hyphenated analytical techniques such as GC-MS, where the response in ion counts arriving at the detector is measured as a function of retention time and mass/charge. In fact, data provided from a MS-Sensor should be arranged as multi-way array where the first mode represents samples, the second one corresponds to mass spectra and the third to the elution profiles. Common pattern recognition algorithms applied on MS-Sensor data make use of the averaged mass spectra along the detected peak. That means that the three-way nature of data response is reduced to a matrix holding each sample measurement in its row and different m/z channels in columns. Exploiting differences in the time response of the analytes can enhance the subtle variations in the spectra. A potentially powerful approach to analyzing time-dependent data is through the use of multiway or second-order methods, such as NPLS, and PARAFAC. The main goal is to see whether improved quantification or classification can be observed by using second-order methods, even in the case of crude or poor chromatographic separation such direct MS-Sensor devices. To date, no applications of second-order methods to pattern recognition in MS-Sensor devices have been reported in the literature.

2. Goals

This paper is aimed to demonstrate that considering time dimension in the signal provided by a MS-Sensor allows obtaining some extra-information relying on the structure of this data able to produce more reproducible and stable results either in classification and prediction models.

3. Material and methods

Eleven types of Spanish Iberian dry-cured hams obtained from a regular market and differing on the type of food the pigs ate were analysed. Reproducible headspace samples were injected into the injection port of a GC-MS using a headspace autosampler. The system was kept at 200ºC isothermal and chromatographic separation was avoided. Averaged mass spectra along the unresolved peak was then considered as a matrix for further multivariate analysis. The response matrix used for three way analysis was conformed by 66 samples × 76 m/z × 101 scans.

4. Data preprocessing

An important step for the comparison of chromatograms by multivariate modelling was to align the chromatograms derived from each sample. Many of the chemometrics techniques available for multi-way modelling rely on trillinearity, a prerequisite seldom met due to the variations in the chromatographic conditions

affecting peak position and peak width. One way to tackle this problem is to pre-process the data by some kind of time alignment procedure Several methods has been proposed for alignment of second order data where the spectral information is used to guide the alignment procedure All the approaches presented in the references mentioned required from user intervention to set-up the optimal parameters for alignment algorithms.

		TRAINING					TEST		
		# LV's	Var y-block	RMSEC	RMSECV	% Success cross-validation	Var y-block	RMSEP	%Success test
Feeding	NPLS-DA	6	91,520	0,145	0,220	100,00	66,41	0,289	97,73
	PLS-DA	13	99,230	0,059	0,117	100,00	40,362	1,187	100,00
	unf-PLS-DA	11	100,000	0,032	0,337	86,36	52,190	1,063	95,45
Origins	NPLS-DA	10	99,184	0,056	0,403	86,36	56,976	0,404	61,36
	PLS-DA	13	97,848	0,101	0,247	68,18	66,396	1,063	93,18
	unf-PLS-DA	15	100,000	0,011	0,338	81,82	65,111	1,083	77,27
Producers	NPLS-DA	11	99,840	0,068	0,700	55,23	55,225	1,122	74,87
	PLS-DA	13	98,530	0,203	0,387	68,18	60,629	3,335	86,36
	unf-PLS-DA	14	99,912	0,014	0,344	68,18	59,561	2,135	54,55

***Table 3**: Results for PLS-DA and NPLS-DA classifier models for both two and three-way data.*

It is a drawback from a MS-Sensor point of view because it does not allow automatic data processing. Recently, a full automated algorithm called RAFFT (Recursive Alignment Fast Fourier Transform) has been presented by Jason W. H. Wong et al. [1]. This algorithm makes use of the Fast Fourier transform (FFT) for rapid computation of the cross-correlation function that enables alignments between a target sample and samples to be optimized. A modification of the RAFFT algorithm consisting in applying this algorithm for each m/z channel of current sample instead of doing it with the reconstructed TIC signals has been applied to multiway responses from MS-Sensor as shows Figure 1:

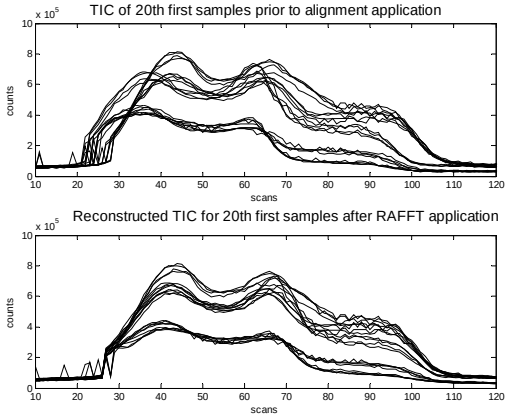

Figure 1: Illustration of RAFFT algorithm performance.

5. Data processing

Different categorization of samples was attempted. First of all a 2-category classification was envisaged regarding two different hams qualities depending on the feeding pig's received during their fattening period either acorn or fodder. A second categorization consisted in to differentiate ham samples according to their different geographical origins namely Extremadura, Guijuelo or Huelva. Finally, the last categorization envisaged was a 5-category classification regarding 5 different producers from which we took the samples. Three different classifier models were calculated for each categorization described above and the performance of these classifiers models were compared. NPLS-DA on the R1 (66×76×101) response data array and PLS-DA on the R2 (66×76) matrix and on the unfolded response matrix R3 (66×7676). Prior to any calculation, data were scaled within second mode (m/z) for both, three and two ways models. In order to assess predictive ability PLS and NPLS models were fitted to R1, R2 and R3 respectively to predict quantitative measurements such as water activity (a_w), relative humidity (%RH) and salt content expressed as (%salt). From the total of 66 measurements performed (six different replicates flask from each one of the eleven different hams), four of these six replicates were used in a calibration step. The number of latent variables was assessed from considering RMSECV in the cross-validation process. Remaining samples not taking part of the training step were used to validate the models. RMSEP and percentage of variance for Y-block were accounted. In case of classification models success rate of classification either for training and validation set were also calculated. Table 1 shows result for different classification purposes and Table 2 summarizes results for predictive models in the prediction for percentage of salt, activity of water and relative humidity.

		TRAINING				TEST	
		# LV's	Var y-block	RMSEC	RMSECV	Var y-block	RMSEP
aw	NPLS	8	96,420	0,007	0,018	71,723	0,020
	PLS	15	99,390	0,003	0,006	40,921	0,028
	unf-PLS	15	100,000	0,001	0,016	68,868	0,021
Salt	NPLS	9	98,960	0,149	0,573	58,952	0,937
	PLS	15	99,482	0,092	0,302	52,766	0,959
	unf-PLS	10	100,000	0,144	0,805	98,084	0,885
RH	NPLS	12	99,880	0,192	2,578	76,419	2,733
	PLS	15	99,483	0,596	1,480	55,859	3,740
	unf-PLS	5	99,691	1,923	2,692	99,544	2,729

***Table 2**: Results for PLS and NPLS predicitver models for both two and three-way data.*

6. Results and discussion

From Table 1 and 2 it can be derived that using multiway approaches allows to fit simpler and more parsimonious models with less tendency to overfitting and able to produce more stable results on prediction of new set of samples unseen by the model.

7. References

[1] Wong, J. W. H., C. Durante and H. M. Cartwright. Anal. Chem 2005, 77, 5655-5661.

Modeling, Verification and Comparison of Short-Channel Double Gate and Gate-All-Around MOSFETs

S. Kolberg, H. Børli, and T. A. Fjeldly

UniK – University Graduate Center and Norwegian University of Science and Technology, N-2027 Kjeller, Norway.

{kolberg,hborli,torfj}@unik.no

Abstract

Models for short-channel DG and GAA MOSFETs are presented. The 2D device electrostatics in the subthreshold regime is dominated by the capacitive coupling between the electrodes, which is analyzed in terms of conformal mapping techniques. In the strong inversion regime, the device behavior is dominated by the inversion charge, permitting the use of a 1D analysis. The models are verified by comparison with numerical device simulations. The properties of the DG and GAA are compared, demonstrating the superior short-channel behavior of the GAA design.

1. Introduction

Nanoscale double gate (DG) and cylindrical gate-all-around (GAA) MOSFETs have been identified as strong candidates for replacing the conventional bulk MOSFET in the coming five to ten years [1]. A major impetus for this advance is the improved gate control and the concomitant reduction in short-channel behavior offered by these device designs.

As an integral part of this development, precise compact models are needed for the DG and GAA MOSFET for implementation in circuit simulators and circuit design tools. To achieve the needed accuracy, the two-dimensionality of the potential and inversion charge distributions has to be taken into account. Especially in the subthreshold regime of operation, the electrostatics in the device body is dominated by the 2D capacitive coupling between the source, drain and gate electrodes. For the DG MOSFET, the Laplace's equation can be solved in different ways. One possibility is to perform a full Fourier expansion of the potential or by using a low-order truncation [1-4]. We have found the conformal mapping method to be particularly suitable for analyzing this regime [6-12]. The GAA MOSFET, which is basically a 3D structure, cannot be analyzed directly the same way. One possibility is to solve Poisson's equation in cylindrical coordinates by means of a series expansion in Bessel functions [5]. Here we show that the above analytical results from the DG structure can be applied to the GAA as well, by performing an appropriate compensation for the difference in gate control. The results verified by comparisons with numerical device simulations from the Silvaco's Atlas device simulator.

2. 2D capacitive coupling

The potential distribution owing to the capacitive coupling between the source, drain and gate contacts in the DG MOSFET can be obtained by solving the 2D Laplace equation by means of the conformal mapping technique. This solution then applies to the subthreshold regime, where the capacitive coupling dominates the electrostatics. The first step is to map the cross-section of the device body (see Fig. 1a), defined in the normal (x,y)-plane, into the upper half of a complex (u, iv)-plane (see Fig. 1b) by means the following Schwartz-Christoffel transformation [6].

We therefore adopt the electrostatics of the DG MOSFET and apply it to a GAA MOSFET with an adjusted geometry to compensate for their difference in gate influence on the body. Important parameters in this procedure are the so-called characteristic lengths of penetration of electrostatic influence from the source and drain towards the device center for the DG and GAA geometries. These are given by in [16,17].

3. Results and discussions

The small dimensions of the present devices indicate that the drain current will have the character of both drift-diffusion and ballistic/quasi-ballistic transport. Here, we discuss a drain current model based on the classical drift-diffusion formalism. For both devices, we find that for subthreshold conditions the barrier topography is relatively rigid, i.e., it is little affected by the drain current. This allows us to use the simple, explicit drift-diffusion model for the current that relies on the shape of the barrier near its maximum [18] For the strong inversion regime we adopt the solutions in [13, 14].

4. Conlusions

We have developed a precise, compact 2D model for calculating the electrostatics as well as the drain currents in nanoscale DG and GAA MOSFETs. The 2D modeling is based on conformal mapping techniques and a self-consistent analysis of the energy barrier topography, that include the effects of both the

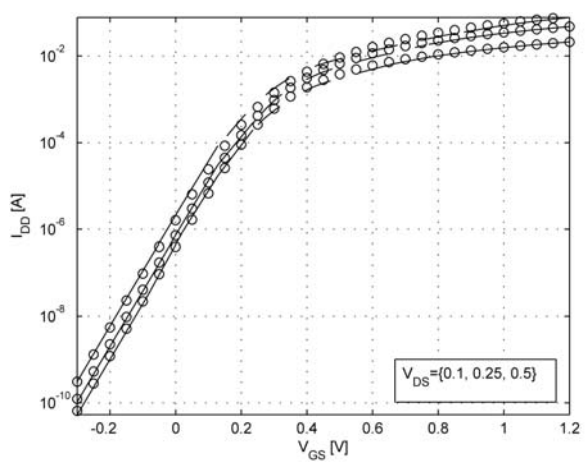

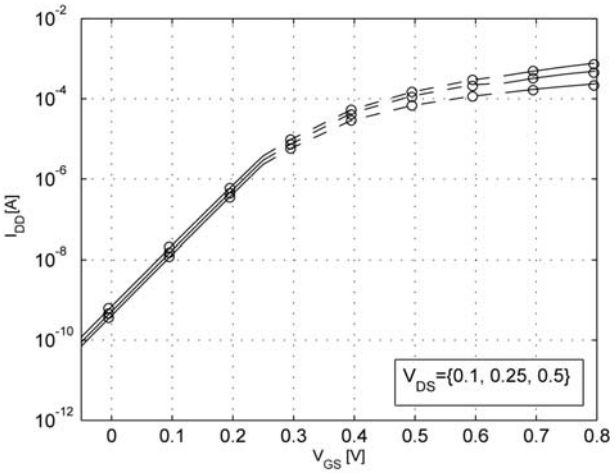

Fig. 1: Drift-diffusion current for DG MOSFET (a) and GAA MOSFET (b) versus VGS for VDS = 0.1 V, 0.25 V and 0.5 V. Comparison between calculations based the present model (solid curves) and numerical simulations performed with Atlas (symbols).

capacitive coupling between the contacts and the presence of electrons. Short-channel effects, including DIBL, are inherently contained in this analysis, and no adjustable parameters are used. The models also include strong inversion solutions based on the dominance of the inversion charge on the device behavior. Assuming a drift-diffusion transport mechanism, the drain current calculated from the present models and from numerical simulations (Silvaco Atlas) show excellent agreement. The superior gate control of the GAA is demonstrated through comparisons with the DG device.

Acknowledgements

This work was supported by the European Commission under contract no. 506844 (SINANO) and the Norwegian Research Council under contract No. 159559/130 (SMIDA). We acknowledge the donation of TCAD tools from Silvaco and would like to thank Prof. Benjamin Iniguez from Universitat Rovira i Virgili, Spain for helpful discussions.

References

[1] Woo, J. S., Terrill, K.W., Vasudev, P. K.: Two-dimensional analytic modeling of very thin SOI MOSFETs. IEEE Trans. Electron Devices. vol. 37 (1990) 1999-2005

[2] Frank, D. J., Taur, Y., Wong, H.-S. P.: Generalized scale length for two-dimensional effects in MOSFETs. IEEE Electron Device Letters. vol. 19 (1998) 385-387

[3] Oh, S.-H., Monroe, D., Hergenrother, J. M.: Analytic Description of Short-Channel Effects in Fully-depleted Double Gate and Cylindrical, Surrounding-Gate MOSFETs. IEEE Electron Device Letters. vol. 21. no. 9 (2000) 1173-1178

[4] Liang, X., Taur, Y.: A 2-D analytical solution for SCEs in the 2D MOSFET. IEEE Trans. Electron Devices. vol. 51. no. 8 (2004) 1385-1391

[5] Hamid, H. A., Iñíguez, B. Jiménez, D., Roig, J., Pallares, J.,Marsal, L. F.: Two-dimensional analytical theshold voltage roll-off and subthreshold swing for undoped culindrical gate all around MOSFET. Solid-State Electronics. Vol. 50 (2006) 805-812

[6] Weber, E.: Electromagnetic fields, vol. 1 - Mapping of Fields. Wiley, New York (1950)

[7] Klös, A., Kostka, A.: A new analytical method of solving 2D Poisson's equation in MOS devices applied to threshold voltage and subthreshold modeling. Solid-State Electronics. vol. 39 (1996) 1761-1775

[8] Østhaug, J., Fjeldly, T. A., Iniguez, B.: Closed-form 2D modeling of sub-100nm MOSFETs in the subthreshold regime. J. Telecom. and Information Techn. vol. 1/2004, (2004) 70-79

[9] Kolberg, S., Fjeldly, T. A.: 2D modeling of nanoscale DG SOI MOSFETs in the subthreshold regime, J of Comput Electron. vol.5 (2006) 217-222

[10] Kolberg, S., Fjeldly, T. A.: 2D Modeling of Nanoscale Double Gate SOI MOSFETs Using Conformal Mapping. Physica Scripta. vol. T125 (2006) 1-4

[11] Fjeldly, T. A., Kolberg, S., Iñiguez, B.: Precise 2D Compact Modeling of Nanoscale DG MOSFETs Based on Conformal Mapping Techniques, Proc. of the Workshop on Compact Modeling, Boston, MA (2006) 668-673

[12] Kolberg, S., Fjeldly, T.A., Iñiguez, B.: Self-consistent 2D Compact Model for Nanoscale Double Gate MOSFETs. Lecture Notes in Computer Science. vol. 3994/2006, (2006) 607– 614

[13] Taur, Y., Liang, X., Wang, W., and Lu, H.: A continuous, analytic Drain-Current Model for DG MOSFETs, IEEE Electron Device Letters, vol. 25, (2004), 107-109

[14] Iñiguez, B., Jiménez, D., Roig, J., Hamid, H.A., Marshal, L.F. and Pallarès, J.: Explicit Continuous Model for Long-Channel Undoped Surrounding Gate MOSFETs, IEEE Trans. on Electron Devices, vol 52, (2005) 1868-1873.

[15] Template device for modeling and simulation defined within the European Commission Network of Excellence project SINANO (http://www.sinano.org/).

[16] Suzuki, K., Tosaka, Y., Tanaka, T., Horie, H and Arimoto, Y.: Scaling Theory for Double-Gate SOI MOSFETs, IEEE Trans. Electron Devices, vol. 40, (1993) 2326-2329

[17] Auth, C. P. and Plummer, J. D.: Scaling Theory for cylindrical fully depleted, surrounding gate MOSFET. IEEE Electron Dev. Letters, vol. 18, (1997) 74-76

[18] Fjeldly, T. A., Shur, M. S.: Threshold Voltage Modeling and the Subthreshold Regime of Operation of Short-Channel MOSFETs. IEEE Trans. Electron Devices. vol. 40, (1993) 137-145

Fabrication and characterization of porous alumina membranes

L. Vojkuvka*, L.F. Marsal , J. Ferré-Borrull and J. Pallarés

Rovira i Virgili University, ETSE-DEEEA

*Tel.: 977 55 87 64 - e-mail:lukas.vojkuvka@urv.cat – http://www.urv.es

Abstract

The samples of self-ordered porous alumina membranes (PAMs) were fabricated by using a two step anodization. The morphology of PAMs was examined by scanning electron microscopy and hexagonally ordered arrays of nanopores were observed. We report on the structural and optical properties PAMs annealed at the different temperatures. The structural properties studied by X-ray diffraction showed out that the porous alumina is crystallized from amorphous phase to gamma and alpha forms during the annealing at 600 ºC up to 1200 ºC. The optical transmission spectra of PAMs with different thickness of 9, 24 and 45 μm and annealed at different temperatures (600, 800 and 1000 ºC) were performed in the wavelength range of 300 – 1000 nm. The results were analyzed and compared with numerical simulations. From these optical measurements we extract the refractive index and extinction coefficient.

1. Introduction

Porous alumina membranes (PAMs) have been intensively studied in the last decades [1]. The PAMs with highly ordered nanopores are produced by a two step electrochemical procedure [2] and provide a wide range of potential applications in the many fields [3,4].The morphology of PAMs can be modified by adjusting the parameters of anodization so that one can obtain a nanoporous structure with interpore spacings in the range of 50 to 400 nm and pore sizes between 20 and 300 nm. When porous alumina is exposed to high temperatures, different phases of porous alumina are observed. Previous researches have focused in both the study of optical [5] or structural properties of PAMs [6] while in this work we report on optical and structural characterization of PAMs annealed at different temperatures. Once, having these results, we aim at gaining a better insight of the optical properties of porous alumina and its possible application in the future work.

2. Experimental part

High purity 99.999% aluminum foils from Goodfellow Cambridge Ltd. were used as the working substrates. First, the foils were annealed in nitrogen (N_2) at 400 ºC for 3 hours. Next, the sample was electropolished in a 4:1 mixture (volume ratio) of ethanol and $HClO_4$. Then a 2-step anodization was performed in order to create self-ordered porous alumina on the aluminum surface [2]. The first anodization was done in various solutions such as sulfuric or oxalic acid. The potenciostatic regime with different potentials was applied. Then, the porous alumina was removed by a wet chemical etching in a mixture of 0.4 M phosphoric acid and 0.2 M chromic acid at 60 ºC. The second anodization consisted in repeating the same conditions as the first, but changing the runtime to obtain different porous alumina thickness. Finally, the sample was immersed in an ethanol + perchloric acid (1:1) solution cooled to 5 ºC and a voltage of 15 V higher than anodizing voltage was applied in a short pulse (2-3 s) in order to separate porous alumina membrane [7].

3. Results and discussions

The morphology of the PAMs was examined by scanning electron microscopy (SEM). Figure 1 shows the SEM images of the porous alumina structure (PA): A-surface image of PA prepared in oxalic acid, B-cross-section of PA, C- surface image of PA prepared in sulfuric acid and D-bottom part of PA. The surface SEM images showed out hexagonally ordered arrays of nanopores with pore diameter varying from 15 to 40 nm and the interpore spacing from 50 to 120 nm for sulfuric and oxalic acid, respectively.

Figure 2 presents the x-ray diffraction spectra (using Siemens D5000 diffractometer) of PAM annealed in-situ from ambient temperature up to 1200ºC. The diffraction spectra of ambient and annealed at 600 ºC showed out an amorphous structure. The annealing temperatures in the range from 850 up to 1000 ºC transform the PAM structure to a mixture of γ- and σ - phases. However as the temperature increases more γ - alumina peaks appear, while the σ - form is suppressed. The crystallization of PAM to α-phase begins at 1100 ºC and ends at 1200 ºC, when relatively pure α-alumina is obtained.

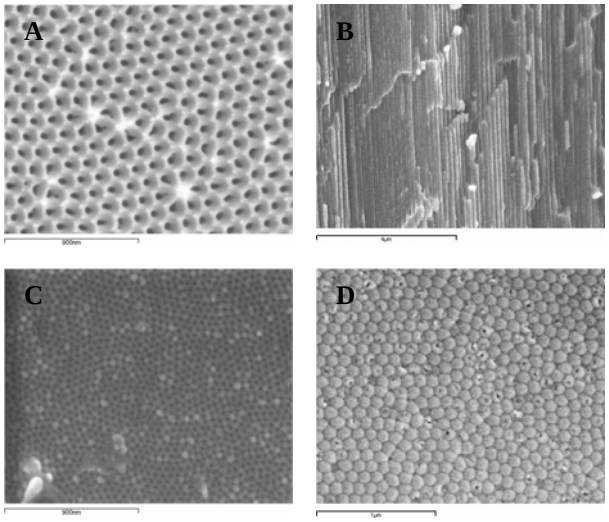

Fig. 1: SEM image of ordered porous alumina (PA). A-surface image of PA prepared in oxalic acid, B-cross-section of PA, C-surface image of PA prepared in sulfuric acid and D-bottom part of PA.

The ordered porous alumina membranes with the different thicknesses (9, 24 and 45 μm) and for the different annealing temperatures (as produced, 600, 800 and 1000 ºC) were analyzed with a spectrophotometer with a SpectraPro-150 monochromator from ARC Inc. in the wavelength range from 300 to 1000 nm.
The transmittance spectra were analyzed by a standard optical characterization method [8]. This permits to obtain the value of refractive index and extinction coefficient for the porous alumina samples obtained after annealing at given temperature.

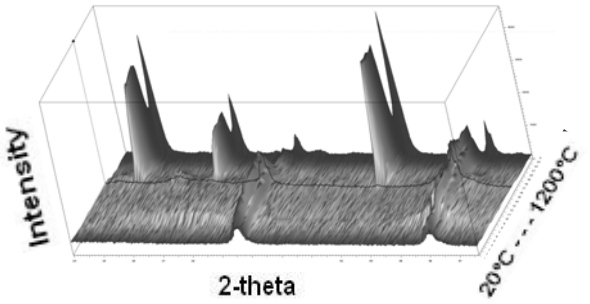

Fig. 2: 3-D diffraction spectra measured in-situ by increasing the temperature up to 1200ºC.

The transmittance measurements are shown in Figure 3(a-c). The spectra show a nearly constant value varying between 80 – 90 % in the wavelength range from 500 nm to 1000 nm. In the range from 300 nm to 500 nm an absorption peak can be observed.
The corresponding refractive index and extinction coefficient for the different annealing temperatures are shown in Fig. 3d. In all cases the refractive index n is constant with wavelength with values of 1.52, 1.54, 1.55 and 1.62 for as-produced, 600 ºC, 800 ºC and 1000 ºC, respectively. The extinction coefficient curves for the as-produced and the 600 ºC annealed sample show one single maximum around 400 nm while for the samples annealed at 800 and 1000 ºC show two maxima.

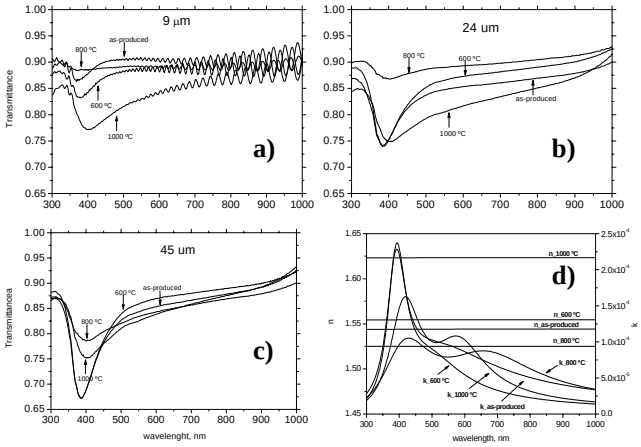

Fig. 3: Transmittance spectra of PAMs with different thickness (9, 24 and 45μm) and annealed at different temperature of 600, 800 and 1000ºC – a, b and c. The refractive index *n* and extinction coefficient *k* are presented in figure d.

4. Conlusions

The ordered porous alumina membranes (PAMs) were fabricated using 2-step anodization.. The structural properties of PAMs were analyzed by X-ray diffraction. The crystallization starting from amorphous phase at ambient temperature, passing through γ-alumina between 800 – 1000 ºC and finally reaching α-alumina form at 1200 ºC was observed. The refractive index and extinction coefficient of PAMs were obtained in the wavelength range from 300 to 1000 nm.

Acknowledgements
This work was supported by the Spanish Commission of Science and Technology (MEC) under grant number TEC2005-02038. J. Ferré acknowledges the Ramon y Cajal fellowship from the Spanish Ministerio de Ciencia y Tecnología.

References

[1] F. Keller, M. S. Hunter and D. L. Robinson, J. Electrochem. Soc., 100 (1953) 411
[2] H. Masuda, K. Fukuda, *Science*, 268 (1995) 1466
[3] K. Nielsch, R. B. Wehrspohn, J. Barthel, J. Kirschner, U. Gösele, S. F. Fischer, and H. Kronmüller, *Appl. Phys. Lett*., 79 (2001) 1360-1362
[4] G . Che, B. B. Lakshmi, E. R. Fisher, C. R. Martin, *Nature*, 393 (1998) 346
[5] Y. Du, W. L. Cai, C. M. Mo, J. Chen, L D. Zhang and X. G. Zhu, *Appl. Phys. Lett*., 74 (1999) 20
[6] P. P. Mardilovich, A. N. Govyadinov, N. I. Mukhurov, A. M. Rzhevskii and R. Paterson, *J. Mem. Science*, 98 (1995) 131-142
[7] J. H. Yuan, F. Y. He, D. C. Sun and X. H. Xia, *Chem. Mater*., 16 (2004) 1841-1844
[8] S. Bosch, J. Ferré-Borrull and J. Sancho-Parramon, *Solid-StateElectronics*, 45 (2001) 703

Synthesis of sensing composite SnO_2-SiC using one dimensional SiC nanostructures.

R.G. Pavelko[1,2], A.A. Vasiliev[1,3], X. Vilanova, V.G. Sevastyanov[2]

[1] University Rovira i Virgili, Av. Paisos Catalans, 26, Tarragona, Spain
[2] Institute of General and Inorganic Chemistry, RAS, Leninskiy prosp., 31, Moscow, Russia
[3] RRC Kurchatov Institute, Kurchatov sq. 1, 123182, Moscow, Russia
rpavelko@yandex.ru, A-A-Vasiliev@yandex.ru, xavier.vilanova@urv.cat, v_sevastyanov@mail.ru

Abstract

In this article we report about synthesis and characterization of SiC-SnO_2 composites used for preparing advanced sensing material for combustible gases. The synthesis condition allow to obtain one dimensional silicon carbide structures (so called "whiskers") and to precipitate onto SiC surface tin dioxide particles with average crystallite size 7 nm. Characterization of obtained material was carried out by means of TEM, X-Rays diffraction and optical microscopy. It was found also separate silicon carbide whiskers covered with tin dioxide particles what allows us to suppose that surface of SiC whiskers was a nucleus of crystallization for growing SnO_2 particles. Thus SiC-SnO_2 composite represent a matrix of SnO_2 with SiC skeleton inside the bulk material.

1. Introduction

The sensing properties of semiconductor metal oxide in form of thick or thin films have been studied in improving selectivity and stability for more than 50 years. In 1991 Yamazoe [1] showed that reduction of crystallite size caused a huge improvement of sensor sensitivity/performance.

However, the reducing of particle size is accompanied with drastic increasing of surface energy of sensitive material. Nanoscaled materials aspire to decrease its surface via agglomeration, recrystallization or diffusion in substrate bulk. These effects become more critical because the metal oxide layers must be kept at relatively high temperature in order to guarantee the reversibility of chemical reactions at surface and to decrease the influence of humidity on sensing mechanism [2]. Thus, the problem of long-term stability of nanoscaled sensitive material is a very actually nowadays.

In this work we have tried to use thermal stable and chemical inert compound as a substrate for tin dioxide sensing material. We believe that such type of sensing composite improve long-term stability of nanoscaled tin dioxide. As a chemical inert, physical stable substrate we used one dimensional (1-D) silicon carbide structures. The geometry of the SiC particles is whisker-like what allow to form nanocarcass for precipitated SnO_2.

2. Experimental

SiC nanosubstrate

The synthesis of the silicon carbide nanowhiskers was carried out according to [3]. The starting mixture C+SiO_2 was heated in Ar atmosphere up to 1300^{O}C with temperature rate 50^O/hour. Carbothermal reduction of SiO_2 was realized at 1300^{O}C for 3 hours.

Obtained product was maintained in a furnace at 1200^{O}C under flowing air in order to remove residual carbon and then treated by HF to remove silica and other impurities. To separate nanocrystals with the same geometry we ground nanowhiskers in a mortar and dispersed obtained powder in water by means of ultrasonic generator. After several hours a suspension was obtained consisting of SiC nanoparticles of the same morphology which was used as inert substrate for SnO_2 sensitive material.

Sensitive material

For the fabrication of semiconductor sensing layer we used precipitation of SnO_2 from $Sn(CH_3COO)_4$ solution in acetic acid (Sigma Aldrich). The precipitation was carried out directly onto the SiC nanocrystals using slow evaporation with stirring.

Palladium and platinum catalysts were deposited onto this SiC-SnO_2 carrier by impregnation with $Pd(NH_3)_4(NO_3)_2$ and $Pt(NH_3)_4(NO_3)_2$ (Sigma-Aldrich) and following annealing at 650^{O}C. Concentration of Pd was equal to 3 wt.% and Pt – 1wt.%. The sensing powder after annealing was stirred with organic vehicle (ethyl cellulose in terpineol) to get homogeneous printable ink.

3. Results and discussion

Due to realization of transport conditions of SiC in gas phase [3] we obtained continuous 1-D SiC

structures. An optical microscopy photograph of the material is given in Figure 1a.

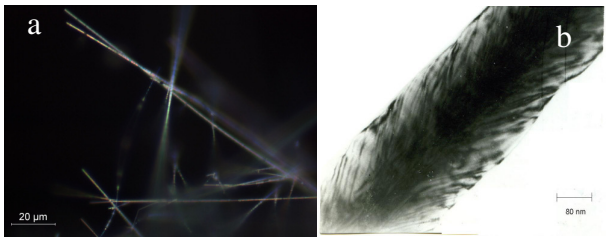

Fig. 1. (a) - Optic photograph of SiC nanowhiskers (C. Zeiss 500x); (b) - TEM photograph of separate β-SiC nanocrystal (Jeol 125000x).

Analysis of the crystalline topography was carried out by means of TEM. The silicon carbide nanowhiskers are monocrystals of β-SiC over 1 mm lengthways and from 50 to 250 nm in diameter (Fig. 1b).

The X-ray diffraction showed the crystalline structure of SnO_2-SiC composite (Fig. 2). Two phases can be marked out – cassiterite SnO_2 and β-SiC. The average crystallite diameter for SnO_2 was calculated by means of LVol-IB (Length Diffraction Column Volume Integral Breadth) method and was found 6,7 nm. As it can be seen from X-rays data the β-SiC phase has a peak much more narrow and calculated crystallite size is equal 90 nm which well correlate with the average dimensions of SiC monocristals.

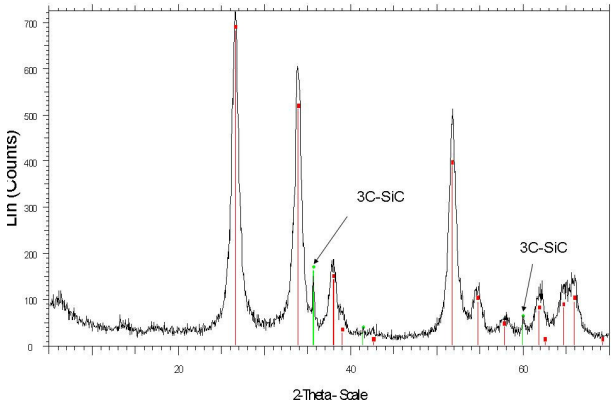

Fig. 2. X-Ray diffraction of precipitated SnO_2 onto β-SiC nanocrystals.

The optical photographs show that SiC nanowhiskers were covered with tin dioxide particles (marked with arrows Fig. 4). The average length of such structures is about 6 µm and the average diameter is 1-2 µm. However the majority of the whiskers being a nucleus of crystallization are hidden inside of SnO_2 particles and can not be seen with optical microscope.

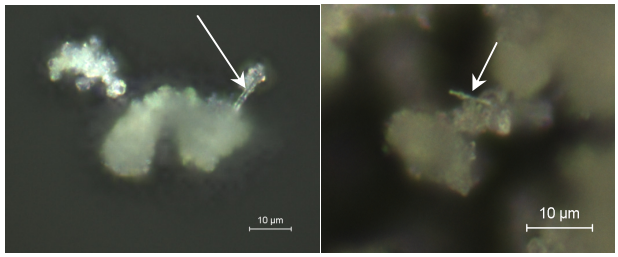

Fig. 3. Optical photograph of SiC-SnO_2 composite. SiC crystals covered with SnO_2 particle (C.Zeiss 700x).

We believe that the presence of second crystalline phase in sensing material as inert and stable silicon carbide will stabilize semiconductor's phase and prevent process of SnO_2 recrystallization. Analysis of sensor long-term stability and sensitivity to combustible gases will present in our further works.

3. Conclusions

We synthesized SiC nanowhiskers using carbothermal reduction of ultradispersed silica. These 1-D structures were used as an inert and thermal stable substrate for tin dioxide nanoparticles. The precipitation of SnO_2 was carried out directly onto silicon carbide surface. The obtained material represents composite-like structure with SiC linear crystals in the bulk of SnO_2 matrix. The calculated average dimension of SnO_2 crystallite is over 7 nm and for SiC is 90 nm.

References

[1] N. Yamazoe, Sens. Actuators B 5 (1991) 7.

[2] D. Kohl, "Surface processes in the detection of reducing gases with SnO2-based devices," *Sens. Actuators*, vol. 18, pp. 71-113, 1989.

[3] V.G. Sevastyanov, R.G. Pavelko, Yu.S. Ezhov, N.T. Kuznetsov "Thermodynamic analysis of synthetic potentialities of the nSiC + SiO_2 starting system; SiC gas-phase transport via Si(g) and CO(g)", *Proceedings of 11th International Conference on Silicon Carbide and Related Materials, Pittsburg, USA*, 2005.

Polymer Waveguides Fabrication and Test

Lorena Diéguez[1], Nasser Darwish[1], Mauricio Moreno[1], Mª Jesús López[2], Josep Samitier[1]
Departament d'Electrònica, Universitat de Barcelona, Martì i Franqués 1, Barcelona, Spain
Plataforma de Nanotecnología, Parc Científic de Barcelona, Josep Samitier, 1-5,Barcelona, Spain
ldieguez@el.ub.es, ndarwish@el.ub.es ,moreno@el.ub.es

Abstract

In this paper the results for the characterization of two polymers, PMMA and SU-8 like films in three layers waveguides are presented. To fabricate and test these waveguides we have used standard lithography and the prism coupler technique. After this, we will design a biosensor knowing that any change in the optical properties of the external medium will be detected by the evanescent wave, and it will affect the propagation properties, so the coupling angles will change.

1. Introduction

An optical waveguide consist in a film with a refraction index higher than the index of the two mediums around. The light travels confined inside the film because of the total internal reflections (TIR)[1]. The light is guided only in a discrete collection angles allowed by the constructive interference conditions [2]. Each propagation relation with each angle is called guided mode. If the effective refraction index, N, is defined like:

$$N = n_f \sin\theta \qquad (1)$$

the values for the guided modes are in the region:

$$n_s < N < n_f \qquad (2)$$

Some modes can travel along the structure depending on the refraction index and the film thickness. Solving the wave equation in three layers planar waveguides it is shown that EM fields have sinusoidal behaviour in the film and exponential fall in the mediums around. Thus, the light is not completely confined in the film. The sensors will use this "evanescent wave principle" [1].

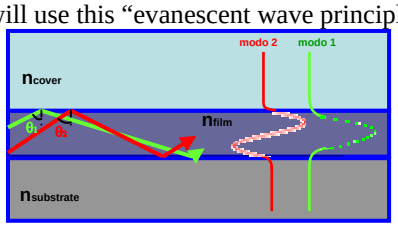

Fig. 1. Three layers waveguide.

2. Fabrication. Thin Layers Deposition

There are two options to work with waveguides: dielectrics and polymers. Dielectrics are very stables and high quality, but polymers are easy handled and low cost.

A. PMMA

The waveguides are fabricated in PMMA, n_f=1.492, over PYREX 1X1 inch, n_s= 1.47. The PMMA is deposited by spin coating getting thin layers [3].

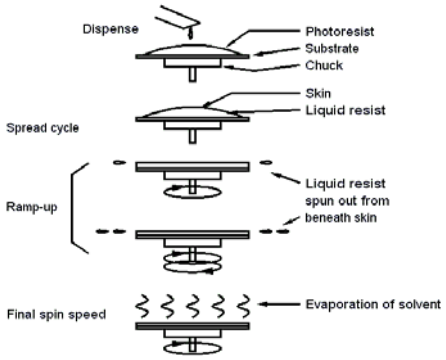

Fig. 2. Spin coating.

The final polymer thickness depends on its viscosity and on the spin speed as is shown in the table I [4]:

TABLE I- EXPECTED PMMA THICKNESS VS SPIN SPEED

Spin Speed (rpm)	Film Thickness (μm)
1000	5
1500	3.7
2000	3
3500	2

Finally, the softbake is done at 180ºC during 60s.

B. SU-8

With the SU-8, n_f=1.596, we have done samples over PYREX and over CROWN, n_s=1.519, to get monomode waves [5].

TABLE II- SU-8 THICKNESS VS SPIN SPEED

Spin Speed (rpm)	Film Thickness (μm)	Material del sustrato
1000	30	PYREX
1500	20	PYREX
2000	15	PYREX
2500	12	PYREX
3000	10	PYREX
8000	4.3	CROWN

Then, is done the pre-bake at 65ºC during 2minutes and the soft-bake at 95ºC during 5minutes.

3. Thin layers Test

Prism coupler

The basic parameters to characterize the films are their refraction index and their thickness. To determinate them we have used the prism coupler technique. Both parameters are obtained simultaneously measuring the coupling angles and fitting them with a theorical

dispersion curve [6].

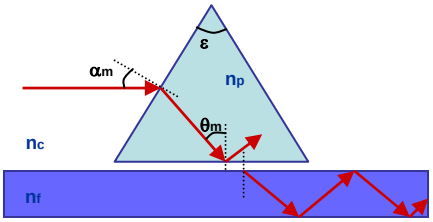

Fig. 5. Prism coupler.

Removing the air gap between the prism and the guide we get that the evanescent field pass through the film. For a determined angle, TIR is produced. Measuring the angles θ that verify the guide conditions, we can find experimentally the propagation constants:

$$\tilde{N}_m = \frac{c}{\upsilon_m} = n_p \sin\theta_m \qquad (3)$$

We can also calculate them by a theorical way, so we only need a computational program to fit both parameters n and W until the theorical values fit to the experimentals, $\bar{n}$ and $\bar{W}$.

The goal of the explained method is that only is necessary the angles measurement. The film has to be thick enough to allow two modes and also it is necessary to press the film mechanically against the prism. Finally, to find the angles requires skill and experience.

We have mounted the prism over a platform xy in a goniometer with an arch minute resolution (Newport) In contact with the equilateral prism (SF11, Thorlabs) we place the sample and press, appearing a spot that will be the coupling point. The He-Ne laser (λ=633nm) is polarized TE and focalised over the spot.

We have measured only the PMMA samples and introduced in our program in MATLAB that gives us a numerical solution:

TABLE IV- PMMA FIT RESULTS

$W_{teórico}$ (μm)	$\bar{n}$	$\bar{W}$ (μm)	σ(n,W)
5	1.4871	5.0687	$4.72\cdot10^{-7}$
3.7	1.4895	3.6187	$6.78\cdot10^{-7}$
3	1.4886	3.1392	$2.15\cdot10^{-5}$
2	1.4886	2.0967	$1.38\cdot10^{-5}$

The obtained results fit perfectly to the expected as we can see in the graph:

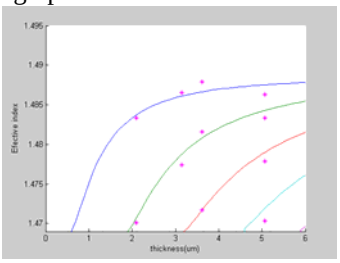

Fig. 7. Theorical and observed effective index curve.

So we can conclude that the film index is n_f=1.4886.

4. Rib Guides. Photolithography

The SU-8 is a negative photoresist, so we have design different masks in Freehand and high resolution printed in transparency. We have painted rib curves and Y couplers with different ratios, amplitudes and thickness. We exposed the samples with the masks to the UV during 2s [3], cured in two steps: post-bake1 at 65ºC during 1min and post-bake2 at 95ºC during 2min. Finally, we dipped the sample in the developer to remove the photoresist in the uncured region.

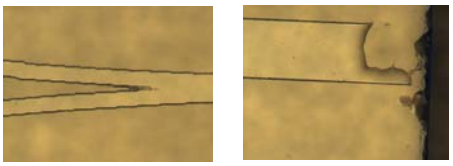

Fig. 10. Metalographic Optical Microscope pictures of the SU-8 samples.

5. Replication

For the replication some silicon nitrure chips (1X1cm) are used as masters, with 3 pairs of gratings etched 20nm deep [7], [8]. These refraction gratings are stamped with Nano Imprint lithography (NIL) at 130ºC during 600s at 30 bar pressure over 1.5 μm PMMA layers spun over 1X1 inch PYREX.

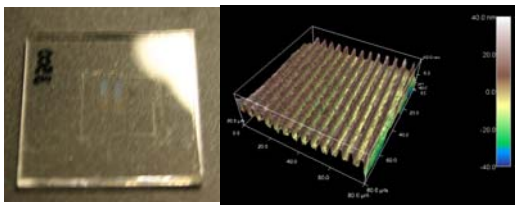

Fig. 11. (Left) Photograph of the gratings replicated in a polymer guide (Right) AFM picture of these replicated gratings.

6. Conclusion

- Knowledge about thin layers spin technique
- Optical test and numerical fit program in MATLAB
- Masks design and fabrication
- Chips etching in polymer by NIL

References

[1] F.Prieto Espuñes, “Sensores interferométricos Mach-Zehnder integrados basados en guías de onda arrow para aplicaciones biosensoras”, Dra.L.M.Lechuga, CNM, CSIC, 2002, pp. 31–37.

[2] IAsys, Technical note 3.1 Background Information. “The Resonant Mirror”, Part No. LAS853010 Issue 3.

[3] D.C.O’Shea, T.J.Suleski, A.D. Kathman, D.W. Prather, “Diffractive Optics. Design, Fabrication, and Test”, 2004, SPIE. pp. 135–137

[4] © MicroChem Corp., NANO™ PMMA and Copolymer. 2001.

[5] © MicroChem Corp., NANO™ SU-8.

[6] R. Ulrich, R. Torge, “Measurement of Thin Film Parameters with a Prism Coupler” Applied Optics, 1973.

[7] C.A.Mills, J.Escarré, E.Engel, E.Martínez, A.Errachid, J.Bertomeu, J.Andreu, J.A.Planell and J.Samitier,“Micro-and nanostructuring of poly(ethylene-2,6-naphthalate)surfaces, for biomedical applications, using polymer replication techniques” Nanotechnology (2005) 369-375.

[8]C.A.Mills, E.Martínez, F.Bessueille, G.Villanueva, J.Bausells, J.Samitier, A.Errachid.“Production of structures for microfluidics using polymer imprint techniques” Microelectronic Engineering (2005) 695-700.

Methods of Modeling and Simulation of Nonlinear Photonic-Crystal Devices

I. S. Maksymov, L. F. Marsal and J. Pallarès

Nanoelectronic and Photonic Systems Group, Departament d'Enginyeria Electrònica, Elèctrica i Automàtica, Universitat Rovira i Virgili, Avda. Països Catalans 26, 43007 Tarragona, Spain. E-mail: lluis.marsal@urv.net

The theoretical investigation of photonic crystal's properties is one of the up-to-date tasks of the scientific community. The calculation of characteristics of the nonlinear photonic crystals is extremely important if all-optical devices are to be designed and analyzed. In this study, existing approaches used for analyzing photonic crystals are classified by considering their mathematical apparatus and then discussed taking into account the applicability to solve different classes of problems.

First of all, these approaches can be mainly divided into four big groups that include the analytical, numerical-analytical, numerical grid and hybrid grid methods. Secondly, the secondary classification can be made by considering what kind of parameters has to be calculated. For example, the calculation of transmission and reflection consists in exploring analytically or numerically the propagation of the electromagnetic waves in finite structures like waveguides, cavities or photonic crystal lattices consisting of finite number of periods. By taking the Fourier transform of the temporal evolution of the field, one obtains the transmission and reflexion spectra. Such an approach corresponds to that used in realistic measurement techniques. In contrast, the dispersion characteristic calculation is carried out for infinite structures where the periodic boundary conditions are imposed to model the periodicity. It is evident that in the reality no measurements can be made to verify theoretical results. However, the information on the structure obtained through the dispersion characteristic calculation really helps in developing optical devices.

The first approach discussed here is analytical. It is borrowed from the solid-state theory where it was widely used to solve the Schrödinger equation. This equation is one of the basics of the solid-state theory and it describes the behavior of a particle in an arbitrary potential. Contrary to that, the photonic crystal analysis is based on the classical Maxwell theory that describes the behavior of a wave packet in a medium. But under particular circumstances wave packets behave like particles thus justifying the application of the analytical approach to solve Maxwell's equations. However it can only be made in one-dimensional case where, due to the complexity of calculations, a lot of simplifications are made to achieve a result. In the linear regime, it is used to obtain both the transmission/reflexion spectra and the dispersion characteristics. In the nonlinear regime this approach is still very useful, but a lot of simplifications should be made.

The numerical-analytical approaches for investigating nonlinear photonic crystals are very useful in calculating dispersion characteristics. The plane wave expansion method is the brightest representative member of this group. It was also widely used in the solid-state theory. The algorithm of the plane wave expansion method has lots of modifications. Other representatives in the group of numerical-analytical approaches are presented in Table 1, which gives the information on their usability.

Considering the popularity of approaches from the following group – the group of the numerical grid methods -, the description here should be started with the finite-difference method [1]. This method is used to analyze both finite and infinite structures of all kinds and geometries. This fact makes it one of the most robustness numerical approaches for analyzing characteristics of photonic crystals. There are two modifications of the finite-difference method. The type of the modification depends on whether the time derivative is considered in the calculation or not. If it is considered, the method should be called by its very famous acronym FDTD [1], which means the "finite-difference time-domain". At the present day, the word "FDTD" means an independent numerical method with tens of modifications and extensions [1]. However, if the time derivative is omitted, the acronym FD or finite-difference is used.

In the FDTD, the Maxwell's equations are discretized in both time and space and then iteratively solved for a finite number of iterations. For instance, in the three-dimensional case all the field components and all the direction in space are considered, which means that the difference between the calculation and the natural electromagnetic field propagation is only due to discretization errors and computation limitations.

Unlike the FDTD method, the FD does not take into account the time derivatives and its algorithm is limited to solution of the Helmholtz equations. One equation contains the electric field vector and another one deals with the magnetic field vector. Here, no iteration process is made because the solution consists in solving a matrix equation, which takes into account the geometry of the photonic crystal and the boundary conditions. The main disadvantage arises when one tries to apply the FD method for computing dispersion characteristics of nonlinear photonic crystals. It is evident, that there is no manner to deal with nonlinearity if the basic equation does not include the electric field vector.

The second representative of the group of numerical grid methods is the finite element method. It is known to be a very flexible and powerful numerical tool due to the possibility to discretize arbitrary computation domains with fine grids of arbitrary configuration. The finite element method is used to calculate both dispersion characteristics and transmission spectra of nonlinear photonic crystal [2]. It was

shown that at the same memory requirements the finite element method is 10 times more complex than the FDTD method. It is the reason why a hybrid approach based on these two methods was proposed. In it, the central part of the computation domain is calculated with the FDTD and the finite element method is applied at the boundaries with a "complex" geometry.

The last group of the approaches for analyzing the characteristics of nonlinear photonic crystal consists of hybrid grid methods. This group includes the method-of-lines, the beam propagation method, the finite-volume time-domain method and the transmission line method. The main attention should be paid to the beam propagation and the transmission line methods. The first of them is known to be a very efficient numerical tool, which is widely used in calculating the characteristic of nonlinear optical devices including photonic crystals. The second method, to the authors' knowledge, was only implemented in one-dimensional nonlinear photonic crystal. Nevertheless, it can be extended to be applied to any geometry.

The comparison of the methods that belong to these four groups reveals that many of them can be applied to model and simulate nonlinear photonic crystal devices. However, each of them suffers from some disadvantages that arise from differences in algorithms and aims for which they were created. There is also one problem common for almost all the methods connected with a lack of universality. For example, the Fourier method was applied only for calculating dispersion characteristics of one-dimensional nonlinear photonic crystals. The Korringa-Kohn-Rostoker (KKR) method has a very complex mathematical apparatus and its program realization is a difficult task. The spherical-wave method is only valid for three-dimensional photonic crystal. Although the plane wave expansion methods and the transfer matrix method are very suitable for calculating dispersion characteristics and transmission spectra, their application is limited because a change in geometry results in a change in the analytical expression in their algorithms. It prevents their application to structures with complex geometries, which cannot be described analytically. The finite element method seems to be universal, but its program realization is difficult because very sophisticated mesh generators must be used.

Unlike all these method, the finite-difference time-domain method looks like the most universal numerical tool for analyzing nonlinear photonic crystals. A review of the up-to-date scientific software market reveals that this method is employed in the most powerful commercial programs such as FULLWAVE, OptiFDTD, Lumerical FDTD, XFDTD, CrystalWave and others. All these packages include models of nonlinear effects in various materials.

The NEPHOS group has its own home-made FDTD simulator [3]. It includes the models of nonlinearity and metals. Fig. 1 shows an example of simulation of a photonic crystal multiplexer.

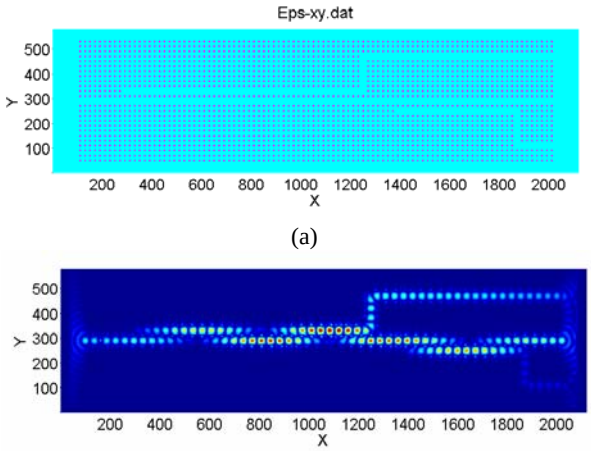

Fig.1. (a) Geometry of the photonic crystal multiplexer and (b) the electric field intensity distribution simulated with the FDTD program.

Conclusions

The methods used for analyzing photonic crystals have been classified by considering their mathematical apparatus and then discussed taking into account the applicability to solve different classes of problems. An example of simulation of a photonic crystal device has been provided.

This work has been supported by MEC, project No. TEC2005-02038

References

[1] A. Taflove and S. Hagness, "Computational Electrodynamics. The finite-difference time-domain method", Artech House, Boston, 2005.

[2] B. Hiett, "Photonic Crystal Modelling using Finite Element Analisys", Ph. D. thesis, University of Southampton, 2002.

[3] I. S. Maksymov, L. F. Marsal and J. Pallarès, "An FDTD analysis of nonlinear photonic crystal waveguides", Opt. Quantum. Electron. 38, 149 (2006).

Table 1. Numerical-analytical approaches.

Method	T/R	Dispersion characteristic	Nonlinearity
Mode expansion	Yes	Yes	Yes
Korringa-Kohn-Rostoker	Yes	Yes	No
Fourier	No	Yes	Yes
Modal	Yes	No	Yes
Integral equation	Yes	No	Yes
Spherical-wave	No	Yes	Yes
Transfer matrix	Yes	Yes	Yes

Compact Model For Doped Double-Gate MOSFETs targeting baseband analog applications

Oana Moldovan[a], Antonio Cerdeira[b], David Jiménez[c], Jean-Pierre Raskin[d], Valeria Kilchytska[e], Denis Flandre[e], Nadine Collaert[f], and Benjamin Iñiguez[a]

[a]Departament d'Enginyeria Electrònica, Elèctrica i Automàtica, Universitat Rovira i Virgili, 43007-Tarragona, Spain
[b]Departamento de Ingeniería Eléctrica, Centro de Investigación y de Estudios Avanzados del I.P.N, 07360-México, D.F.
[c]Departament d'Enginyeria Electrònica, Escola Tècnica Superior d'Enginyeria, Universitat Autònoma de Barcelona, 08193-Bellaterra, Barcelona, Spain.
[d]Laboratoire d'Hyperfréquences (EMIC) and [e]Laboratoire de Microélectronique (DICE), Université catholique de Louvain (UCL), Place du Levant, 3, B-1340, Belgium
[f]IMEC, Kapeldreef 75, B-3001 Leuven, Belgium

Abstract

An analytical and continuous model for a doped double gate SOI MOSFET, in which the channel current is expressed as an explicit function of the applied voltages, is presented targeting the electrical simulation of baseband analog circuits. A unified charge control model is for the first time derived for doped double gate transistors. It is valid from below to well above threshold, showing a smooth transition between the regimes. Small-signal parameters can be obtained from the model. All small signal parameters have an infinite order of continuity. The calculated current and capacitance characteristics show a good agreement with 2D ATLAS numerical device simulations, in all regimes, and also a very good match to FinFET experimental data, in the case of the drain current.

1. Introduction

Double-gate (DG) transistors are considered to be a very attractive option to improve the performance of CMOS devices and overcome some of the difficulties encountered in further downscaling of MOS field-effect transistors into the sub-50 nanometer gate length regime [1]. In the DG MOSFETs, the control of the channel by the gate is stronger than in single gate MOSFETs. This leads to a significant reduction of DIBL, threshold voltage roll-off, off-state leakage and channel-length modulation [2]. In this paper we present a model for the doped double gate MOSFET, which is analytical, explicit and continuous through all regimes of operation (from weak to strong inversion, as well as linear to, saturation). The current expression is based on a unified charge control model, written in terms of charge densities at the source and drain ends [4] and derived for a doped DG MOSFET. We use an accurate explicit expression of the inversion charge densities in terms of the applied bias. No fitting parameters are used in the charge control model.

2. Model and Results

The surface electric field can be written in terms of the mobile charge density (in absolute value) per unit area at each interface, Q, and the depletion charge density per unit area (in absolute value) $Q_{Dep}=qN_At_{Si}$ (t_{Si} being the Si film thickness) whatever x:

$$E_S(x)=\frac{Q(x)+\frac{Q_{Dep}}{2}}{\varepsilon_{Si}} \tag{1}$$

By integrating the Poisson equation between the centre (y=0) and the top surface of the film (y=-t_{si}/2) we get the electric field as a function of the potential difference $\phi_S-\phi_0$ [3], where $\phi_S=\phi(x,-t_{Si}/2)$ is the surface potential and $\phi_o=\phi(x,0)$ is the potential in the middle of the film. It is observed, from numerical simulations, that the difference $\phi_S-\phi_0$ keeps a constant value from the subthreshold region to well above threshold [3].

$$\phi_S-\phi_0=\frac{qN_At_{Si}^2}{8\varepsilon_{Si}}=\frac{Q_{Dep}}{8C_{Si}} \tag{2}$$

This approximation is valid from subthreshold to well above threshold, for low and moderate V_{GS}(~2V) and for all V_{DS} values [3]. Using (1) we obtain the following charge control model:

$$V_{GS}-V_{FB}-V-\left(\frac{Q_{Dep}}{2C_{ox}}+\frac{kT}{q}\log\left[\frac{q^2}{kT}\frac{N_A{}^3}{n_i{}^2}\frac{t_{Si}{}^2}{2\varepsilon_{Si}}\right]\right)= \tag{3}$$
$$=\frac{Q}{C_{ox}}+\frac{kT}{q}\log\left[\frac{Q}{Q_{Dep}}\right]+\frac{kT}{q}\log\left[\frac{Q+Q_{Dep}}{Q_{Dep}}\right]$$

Note that V varies from source to drain [4].

The drain current is calculated as usual from:

$$I_{DS}=\frac{2W\mu}{L}\int_0^{V_{DS}}Q(V)dV \tag{4}$$

From (3) we get:

$$dV=-\frac{dQ}{C_{ox}}-\frac{kT}{q}\left(\frac{dQ}{Q}+\frac{dQ}{Q+Q_{Dep}}\right) \tag{5}$$

Integrating (4) using (5), between Q_s and Q_d (Q=Q_s at source end and Q=Q_d at the drain end), we have:

$$I_{DS}=\frac{2W\mu}{L}\left[2\frac{kT}{q}(Q_s-Q_d)+\frac{Q_s^2-Q_d^2}{2C_{ox}}+\frac{kT}{q}Q_{Dep}\log\left[\frac{Q_d+Q_{Dep}}{Q_s+Q_{Dep}}\right]\right] \tag{6}$$

(Fig.1-2)

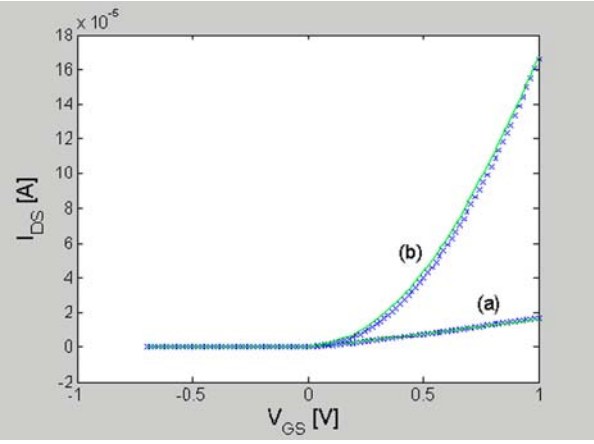

Fig. 1 Transfer characteristics, for V_{DS}=0.05V (a) and for V_{DS}=1V (b) in linear scale. Solid line: Atlas simulation; Symbol line: our model using (6) doping level N_A=6.10^{17}cm^{-3}; silicon thickness t_{Si}=31nm; oxide thickness t_{ox}=2nm; channel length L=1µm and width W=1µm.

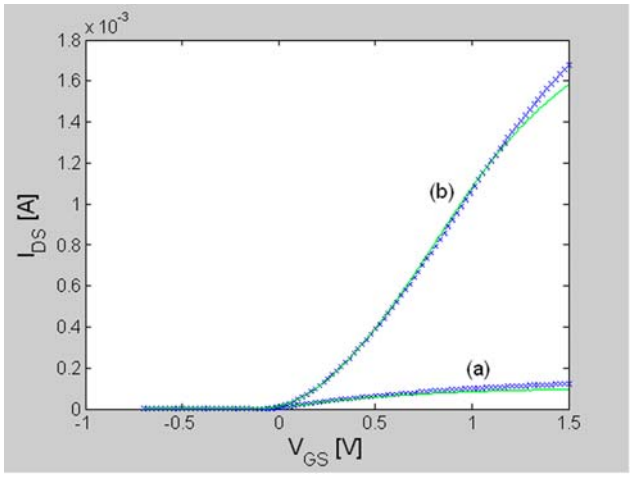

Fig. 2 Transfer characteristics, for V_{DS}=0.05V (a) and for V_{DS}=1V (b) in linear scale. Solid line: FinFET measurements; Symbol line: our model using (6) with FinFET extracted parameter values doping level N_A=1.10^{18} cm^{-3}; fin width=35nm$_i$; oxide thickness t_{ox}=2nm; channel length L=1µm. 66 fins with a height of h_{fin}=75nm. We have modeled the FinFET as a DG MOSFET

In order to compute the charge densities from an explicit expression of the applied bias, since (3) does not yield a closed form for Q, we use the expression used in surrounding gate MOSFETs [4].

The total inversion charge is calculated as [5]:

$$Q_{Tot} = 2W\int_0^L Q dx = (2W)^2 \frac{\mu}{I_{DS}} \int_0^{V_{DS}} Q^2 dV \qquad (7)$$

The total gate charge Q_G=-Q_{Tot}.

The intrinsic capacitances, C_{gd} and C_{gs}, are obtained as [5](Fig.3): $C_{gi} = -\frac{dQ_G}{dVi}$ (8)

where *i=d,s.* The non-reciprocal capacitances C_{dg} and C_{sg} are obtained as [5](Fig.4): $C_{ig} = -\frac{dQ_i}{dV_G}$ (9)

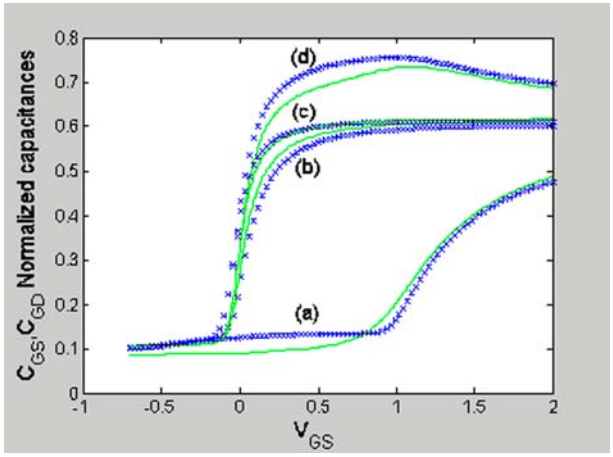

Fig. 3 Normalized gate to drain capacitance (a, b) and gate to source capacitance (c, d) with respect to the gate voltage, for V_{DS}=1V (a,d) and V_{DS}=0.05V (b,c). Solid line: Atlas simulations; Symbol line: our model using (8)

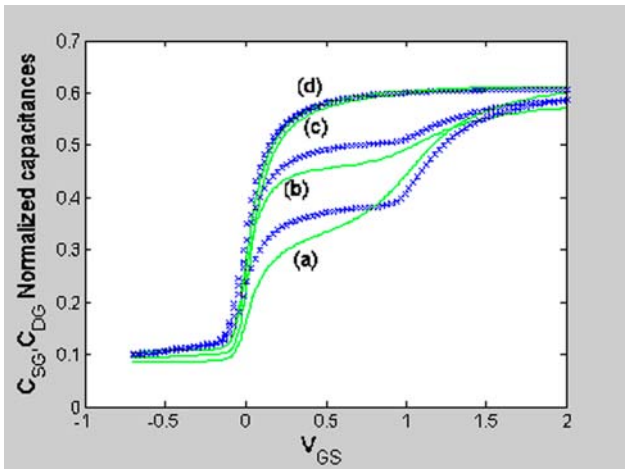

Fig. 4 Normalized drain to gate capacitance (a, d) and source to gate capacitance (b, c) with respect to the gate voltage, for V_{DS}=1V (a, b) and V_{DS}=0.05V (c, d). Solid line: Atlas simulations; Symbol line: our model using (9)

The advantage of our model is that it is charged-based analytical, explicit and continuous through all regimes.

References

[1] Int. Tech. Roadmap for Semiconductors, ed. 2003.

[2] Yiming Li and Hong-Mu Chou. "A Comparative Study of Electrical Characteristic on Sub-10-nm Double-Gate MOSFETs", IEEE Transactions on Nanotechnology, vol.4, no.5, September 2005

[3] Pascale Francis, Akira Terao, Denis Flandre and Fernand Van de Wiele. "Modeling of Ultrathin Double-Gate nMOS/SOI Transistors", IEEE Transactions on Electron Devices, vol.41, no.5, May 1994

[4] Benjamin Iñiguez, David Jimenez, Jaume Roig, Hamdy A. Hamid, Lluis F. Marsal and Josep Pallares. "Explicit Continuous Model for Long-Channel Undoped Surrounding Gate MOSFETs", IEEE Transactions on Electron Devices, vol.52, no.8, August 2005

[5] Benjamin Iñiguez, Luiz Fernando Ferreira, Bernard Gentinne and Denis Flandre. "A Physically-Based C_∞-Continuous Fully-Depleted SOI MOSFET Model for Analog Applications",IEEE TED,vol.43,no.4, April 1996

Quality Factor Enhancement In Metallo-Dielectric Photonic Crystals

M. A. Ustyantsev, L. F. Marsal, J. Ferré-Borrull, and J. Pallarès

Departament d'Enginyeria Electrònica, Elèctrica i Automàtica, ETSE, Campus Sescelades, Universitat Rovira i Virgili, Avda. Països Catalans 26, 43007 Tarragona, Spain
Tel: +34977559625, Fax: +34977559605, e-mail: lluis.marsal@urv.cat

Abstract

We theoretically study the effect of the variation dielectric background on quality factors in two-dimensional metallo-dielectric photonic crystals. characterized by frequency-dependent dielectric function. The metallo-dielectric photonic crystal consists of a square lattice of circular metallic rods embedded into a dielectric background. Results show that the quality factors tend to increase with increasing dielectric constant of background.

1. Introduction

Metallo-dielectric photonic crystals (MDPCs) have already been explored since many years. Despite of the lossy nature of MDPCs these structures have interesting properties. Finally, if the point defect is placed inside photonic crystal different applications can be created like filters [1], polarizer [2], waveguides [3], power splitter [4] or demultiplexer [5]. All these devices are based on metallic scatterers embedded into different dielectric substrates. From a practical point of view, metallic photonic crystals can be realized by electrochemical deposition of a Drude-like material into the holes of a periodic structure of air holes in a dielectric [6].

In this study we present the influence of the variation of the background dielectric constant on the quality factors of metallic photonic crystal. The finite-difference time-domain (FDTD) [7] method is used to accurately calculate the resonant frequencies and quality factors. We show that quality factor and resonance frequencies of defect mode can be tuned either by varying the radius of defect or/and by changing dielectric constant of background.

2. Method and computational model

We used FDTD method combined with the auxiliary differential equations (ADE-FDTD) [7]. The simulation area (Figure 1) consists of 5x5 metallic rods and the radius of the central rod r_d was varied from 0.0a to 0.4a.

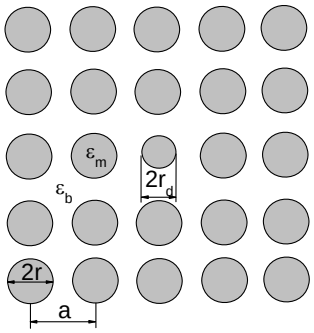

Fig.1. The structure under study. The ε_m and ε_b are dielectric constants of metal and background, respectively. The center rod forms a defect with radius r_d.

The photonic crystal is composed of circular metallic rods in a square lattice with lattice constant a. The radius r of the rods is taken as r = 0.472a. The dielectric constant of the rods is of the Drude model,

$$\varepsilon(\omega) = 1 - \frac{\omega_p^2}{\omega(\omega + i\gamma)}$$

where ω_p is the plasma frequency and γ is the damping term. The parameters were chosen such that $\omega_p a / 2\pi c$ = 1.0 and $\gamma = 10^{-4}\omega_p$. The dielectric constant of the background ε_b was varied from 1 to 12 and was frequency-independent. All simulation were done using a spatial grid resolution 40x40 points per unit cell, with $1 \cdot 10^5$ iterations to achieve convergence. The 15 cells of Convolution Perfectly Matched Layers (CPML) boundary conditions [8] were used on all sides.

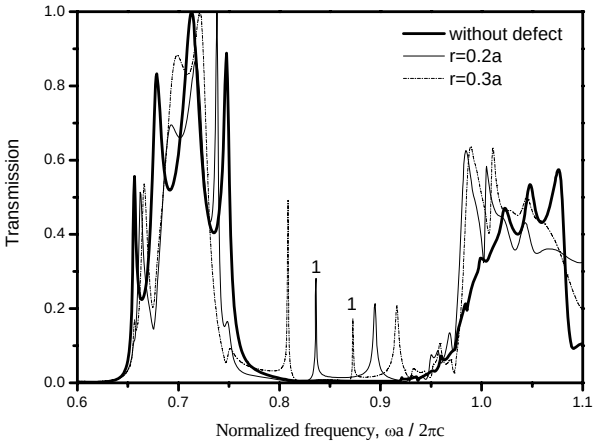

Fig.2. Transmission spectrum of metallo-dielectric photonic crystal with defect rods of different radius when ε_b = 1 (air). The numbers mark resonant frequencies under study.

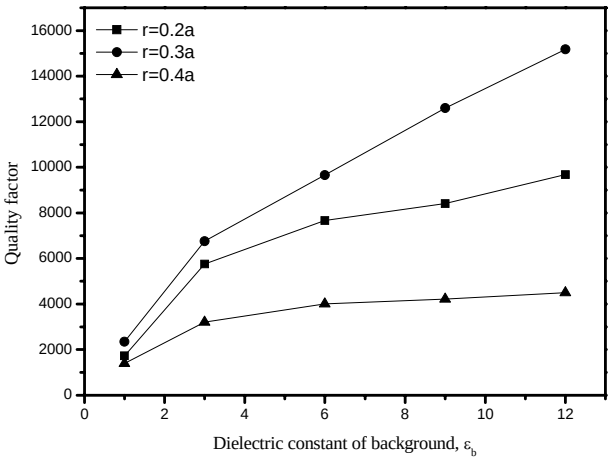

Fig.3. The quality factors as a function of dielectric constant of background ε_b for different radiuses of defect rods.

The structure under study is excited by the Gaussian modulated pulse. The pulse is centered at the 0.7 (in units of $2\pi c/a$) and is broad enough to cover the entire PBG for all ε_b considered here. The transmission spectrum of the photonic crystal is obtained as the ratio between the output and the input intensities.

The quality factors (Q factors) were calculated from the following expression:

$$Q = -\left[\frac{\omega_0 (N_1 - N_0)\Delta t}{2 \ln E_1 / E_0}\right]$$

where ω_0 is resonant frequency of the defect mode, Δt is time-step, E_1 and E_0 are amplitudes at time N_1 and N_0, respectively.

3. Results

Figure 2 shows the calculated transmission spectrums when ε_b =1 for two defects with radiuses r_d =0.2a and r_d =0.3a. We can see the defective modes which appear in the second PBG. When r_d =0.2a the transmission spectrum contains two defective peaks with frequencies 0.8362 ($2\pi c/a$) and 0.8945 ($2\pi c/a$). For r_d =0.3a there are three peaks: 0.8085 ($2\pi c/a$), 0.8726 ($2\pi c/a$), 0.9158 ($2\pi c/a$).

In Figure 3 we plot calculated quality factors as a function of dielectric constants of background ε_b for different radius of defect r_d. As we can see from Figure 3 the Q factors increase with increasing dielectric constant of background and for ε_b =12 Q factors reach 9680, 15180 and 4500 for r_d =0.2a, r_d =0.3a, r_d =0.4a, respectively. It is worth noting that values of Q factors, when ε_b =1, are nearly of the same magnitude and do not depend too much of the defect radius r_d. For example, the Q factors reach 1724, 2348, 1398 when r_d =0.2a, r_d =0.3a, r_d =0.4a, respectively.

4. Conclusions

In this study we have analyzed, by using FDTD technique, the defect modes of two-dimensional metallo-dielectric photonic crystal. We demonstrated that increasing of the dielectric constant of background leads to the increasing of the quality factors in the metallo-dielectric photonic crystals increase.We have also found that quality factors can be tuned either by changing the radius of the defect or/and by varying the dielectric constant of background.

References

[1] C. Xudong, C. Hafner, and R. Vahldieck, Opt. Express **13**, 6175 (2005)

[2] F. Miyamaru, T. Kondo, T. Nagashima, and M. Hangyo, Appl. Phys. Lett. **82**, 2568 (2003)

[3] V. F. Rodríguez-Esquerre, M. Koshiba, H. E. Hernández-Figeroa, and C. E. Rubio-Mercedes, Appl. Phys. Lett. **87**, 091101 (2005)

[4] N. J. Florous, K. Saitoh, and M. Koshiba, Opt. Lett. **30**, 2736 (2005)

[5] J. Choi, G. Sauer, K. Nielsch, R.B. Wehrspohn, and U. Gösele, Chem. Mater. **15**, 776 (2003)

[6] K. Nielsch, R.B. Wehrspohn, S.F. Fischer, H. Kronmüller, J. Barthel, J. Kirschner,

[7] A. Taflove Computational electrodynamics: The Finite-Difference Time-Domain Method, 3rd ed. Norwodd; MA: Artech House, 2005.

[8] J.A. Roden, and S.D. Gedney, Microw. Opt. Technol. Lett. **27**, 334 (2000).

VARIABLE SELECTION FOR SUPPORT VECTOR MACHINES BASED PATTERN RECOGNITION IN MULTISENSOR SYSTEMS

O. Gualdrón **J. Brezmes** **E. Llobet** **X. Vilanova** **X. Correig**

Dept. Enginyeria Electrònica, Universitat Rovira i Virgili, Avda. Països Catalans, 26. 43007, Tarragona, Spain

Abstract

A new variable selection algorithm to be used in SVM pattern recognition applications is proposed. The method is based on weight vector ($||w||^2$) sensitivity against the presence/absence of each variable. The approach is demonstrated using a measurement set of single and binary vapor mixtures. Results show that it is possible to reduce the number of variables without penalizing classification results.

1. INTRODUCTION

In the quest for greater sensitivity and selectivity in multi-sensor systems, the number of parameters to describe each measurement is growing steadily. However, the use of a high number of variables does not necessarily translate into improved performance, since including noisy or irrelevant variables can jeopardise overall results. Instead, choosing the variables that maximize system performance can lead to the design of an optimal sensor array for each particular application [1,2].

Support vector machines are one of the most promising Pattern recognition algorithms for multisensor instruments due to their well founded mathematical base, good generalization ability and robustness against outliers [3-7]. Therefore, we propose a new method to choose the optimal variable subset for Support Vector Machine based pattern recognition in multi-sensor system applications.

2. THEORETICAL BACKGROUND

Support Vector Machine algorithms are binary classifiers that look for an optimal decision hyperplane. SVM's map measurement vector inputs, **x,** into a higher dimensional space using a function, , and then compute a decision function of the form:

$$f(\mathbf{x}) = \langle \mathbf{w} \quad (\mathbf{x}) \rangle + b \qquad (1)$$

This function [8-9] is designed to maximize the distance between key training samples and the decision hyperplane. This hyperplane is parameterized by (w,*b*). In the evaluation stage, the class label of **x** is obtained by considering the sign of $f(\mathbf{x})$ [8-9].

The variable selection method proposed in this paper is based on how the presence/absence of each variable modifies the decision hyperplane. Higher values for the difference between $||\mathbf{w}||^2$ with all variables and $||\mathbf{w}||^2$ without a given variable mean that the variable removed has a strong influence on the decision hyperplane.

The process for the variable selection starts choosing the variable with the largest change in the $||\mathbf{w}||^2$ value when it is removed. Then, the second variable is included and the classification rate computed. The process ends when the addition of newer variables does not improve the classification rate.

3. EXPERIMENTAL RESULTS

Four different concentrations of ammonia, acetone and o-xylene (and their binary mixtures) were measured with an array of 12 metal oxide gas sensors. The data set consisted of 96 measurements which were assigned to 6 different categories according to the species present in the samples. Each category comprised a total of 16 measurements (4 replicates of 4 different concentrations of the same constituents). Since 10 parameters were extracted from each sensor conductance transient (figure 1), the number of variables describing each measurement was 120.

Then, the variable selection process was applied. Figure 2 shows the $||\mathbf{w}||^2$ difference when each variable is removed. The four different lines represent the four iterations in the cross-validation process. As it can be seen, the values are very repetitive through all the iterations even thought the training measurements are not the same.

Since SVM's are binary classifiers, they were executed six times to determine whether a measurement belonged or not to each category. Table 1 shows the success rate achieved for each class and the number of variables needed. It can be seen that, in the worst case, the maximum number of variables needed is 26, instead of 120.

4. CONCLUSIONS

The method presented achieves a 78% reduction in the number of variables needed build classifiers without noticeable performance drop.

Categories	round	Success rate %	# of variables	Success rate % (120 variables)
Cat. 1	A	100	3	100
	B	100	3	100
	C	100	3	100
	D	100	3	100
Cat. 2	A	100	8	100
	B	100	8	100
	C	100	8	100
	D	100	8	100
Cat. 3	A	100	24	100
	B	100	24	100
	C	95.83	24	95.83
	D	100	24	100
Cat. 4	A	95.83	26	95.83
	B	100	26	100
	C	100	26	100
	D	95.83	26	95.83
Cat. 5	A	100	15	100
	B	95.83	15	95.83
	C	100	15	100
	D	100	15	100
Cat. 6	A	95.83	26	95.83
	B	95.83	26	95.83
	C	95.83	26	95.83
	D	95.83	26	95.83

Table 1: Success rate and number of variables for each category in the four different rounds of a crossvalidation of order 4.

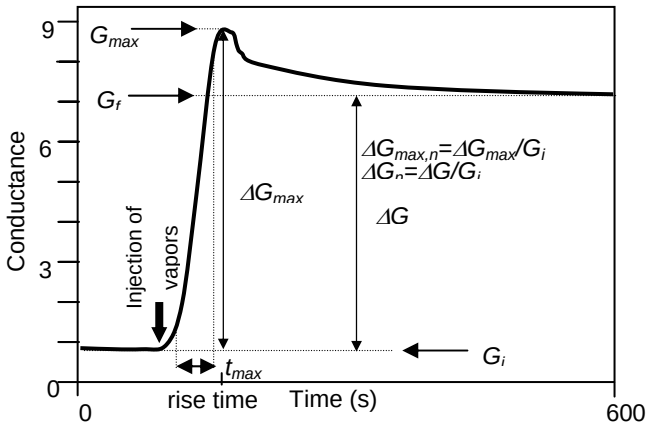

Fig.1 Typical conductance transient response from semiconductor gas sensors and the 10 response features extracted: G_i, G_f, ΔG, ΔG_n, G_{max}, ΔG_{max}, $\Delta G_{max,n}$, t_{max}, $t_{rise10-90\%}$, $t_{rise30-60\%}$

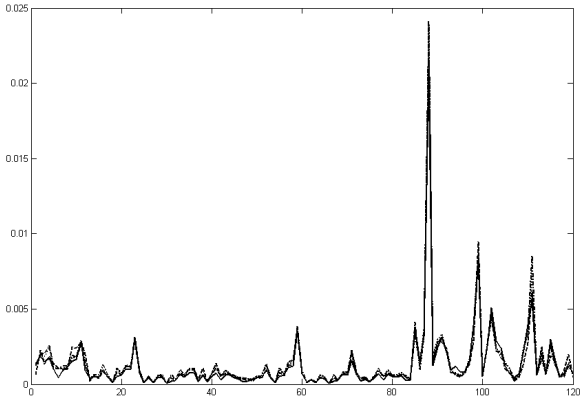

Fig 2: $\|\mathbf{w}\|^2$ difference when each variable is removed. The computation has been done for the classification of category 2 measurements in four rounds. Note the reproducibility of the values obtained.

ACKNOWLEDGEMENTS

This work was funded by CICYT under project no. TIC2003-06301. O. Gualdrón acknowledges a pre-doctoral fellowship from the Universidad de Pamplona, Colombia.

REFERENCES

[1] E. Llobet, J Brezmes, O. Gualdron. X Vilanova, X Correig; Sensor and Actuator B Chemical, 99 (2004), pp 267-272.

[2] J Brezmes, P Cabre, S Rojo, E Llobet, IEEE sensors Journal, (2005) in press.

[3] M Pardo, G Sberveglieri; Sensor and Actuator B Chemical, (2005) in press.

[4] S. Al-Khalifa, S. Maldonado, J. Gardner; IEE Proc-Sci Meas Technol, 150 (2003).

[5] W.H. Land et al.; IEEE international conference on systems, man and cybernetics, Washington DC 2003

[6] D. Martinez, A. Bray; IEEE Transaction on neural networks, Vol 14, no. 1 (2003), pp 228-235.

[7] J. V. Stone, *Neural Comput.*, no. 13, pp. 1559–1574, 2001.

[8] A Rakotomamonjy; Journal of machine learning Research, 3 (2003) pp 1357-1370.

[9] N. Cristianini, J.Shawe-Taylor; Cambridge University Press, Cambridge, 2000

Analysis of 2D-photonic crystal lattice using Bragg-diffraction

Z. Kral*, J. Ferré-Borrull, L. F. Marsal, J. Pallarès

Rovira i Virgili University, ETSE-DEEEA

Avinguda dels Països Catalans 26, Campus Sescelades.43005, Tarragona.
*Tel.: 977 55 86 53 - e-mail: zdenek.kral@urv.net– http://www.urv.es

Abstract

We have investigated an experimental technique to determine the lattice constant of a two-dimensional photonic crystal membrane using Bragg-diffraction measured with a FT-IR spectrometer. The membrane consisted of square air holes electrochemically etched through N-type silicon wafer. The measured data were fitted to a theoretical model to determine the lattice constant. The results were compared with the observation by an optical microscope.

1. Introduction

Photonic crystals have become an attractive structure due to their ability to control lightwave propagation. Photonic crystals are artificial materials with a spatial periodicity of their dielectric constant on a wavelength scale. As was first shown by Yablonovitch [1], geometry and the dielectric constant of the structure dramatically changes the propagation properties of photons inside. In appropriately designed structure, a photonic band gap (a frequency range in which the existence of any electromagnetic modes is forbidden) can be produced. In recent years, most investigations have been concentrated on the fabrication and modeling of photonic crystal materials. Other authors have also investigated on the characterization of the fabricated samples [2,3].

In this paper, we investigate an experimental technique to determine a lattice constant of 2D photonic crystal using Bragg-diffraction. Generally, diffraction occurs when waves are scattered from a periodic structure, such as atoms in a crystal or holes/rods in a periodic photonic crystal lattice. Each scattering center (e.g. each hole or rod) acts as a point source of spherical wavefronts. These wavefronts undergo constructive interference at a given diffraction angle. This angle for a normal incident light can be described by Bragg's law:

$$m\lambda = a \cdot \sin\theta \qquad (1)$$

where λ is the wavelength, a is the distance between scattering centers, θ is the angle of diffraction and m is an integer known as the order of the diffracted beam.

2. Sample optical recognition

Figure 1a) shows the periodic lattice structure of the 2D photonic crystal membrane. The membrane consists of square air holes electrochemically etched through N-type silicon wafer. The pictures are taken with an optical microscope Carl Zeiss Axio Imager A1 with a 50x objective connected to a CCD camera ProgRes C10. The image processing was done using the *i-Solution* (iMTechnology) software. The main crystal directions are indicated and the lattice constant estimated from the picture is 4 μm.

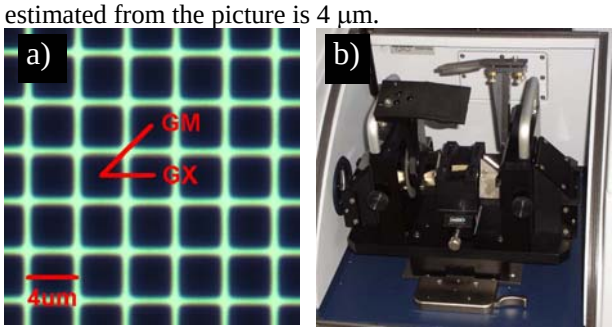

Fig.1. a) Optical microscope picture; the front side of the sample. b) Reflectivity attachment.

3. Experimental part

We have measured Bragg-diffraction using a FT-IR spectrometer (Bruker-Vertex 70) equipped with a special reflectivity attachment (shown in Fig. 1b). The measurement has been performed on the front side of the sample in two directions of incoming light (GX and GM). The light source was a halogen tungsten lamp, the detector was a nitrogen-cooled LN-MCT and the spectral range was from 10000 cm^{-1} to 3000 cm^{-1}. The incoming light was pointed perpendicular to the incident plane (parallel to the hole axis) and the diffraction spectra were measured at angles ranging from 24º to 80º in 2º steps. The specular reflection of the sample for an incidence angle of 12º has been taken as a reference. Fig.2 shows some spectra of Bragg-diffraction for the angles (40º, 42º, 44º, 46º, 48º and 50º).

4. The data analysis

To evaluate the lattice constant, the Bragg-diffraction spectra need to be post-processed.

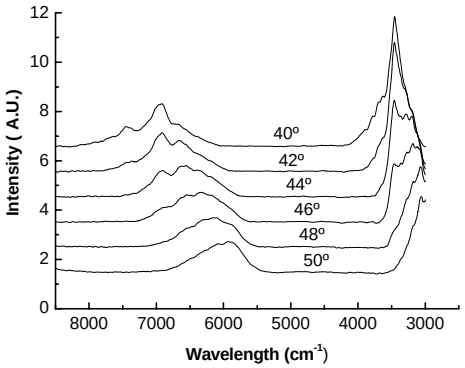

Fig. 2 The Spectra of Bragg-diffraction for some selected angles.

To this end, a Matlab toolbox has been created, which basically includes three steps. The first step consists of performing a moving average of each spectrum to reduce noise. The second step is to consider the dependence of the diffracted intensity with the diffraction angle at each wavelength. For all the wavelengths, the dependence of the intensity with the angle shows a general tendency to decrease with increasing angle. This general tendency is removed by a flattening procedure (fitting the intensity to a straight line and subtracting the resulting straight line from the data). The flattened intensity can be represented with an intensity plot as a function of the wavelength and the diffraction angle, as it is shown in Fig. 3.

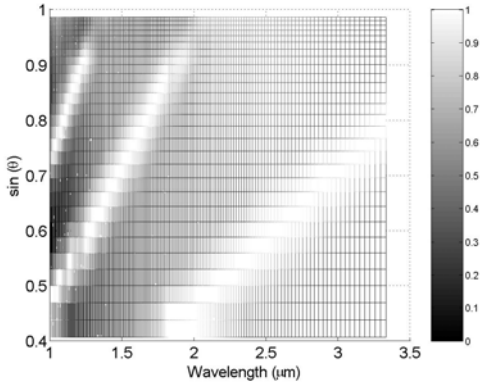

Fig. 3. Intensity plot for GX direction of incoming light. The remaining maxima correspond to the diffraction peaks.

Finally, the third step is to fit a 2-variable function to the flattened data where at least one adjustable parameter is related to the lattice constant. The proposed function is:

$$I(\lambda, sin\theta) = \sum_{n=1}^{3} \exp\left[\left(\frac{sin\theta - \frac{n\lambda}{a}}{w_n}\right)^2\right] \qquad (2)$$

where w_n take into account the width of the diffraction peaks and a for the lattice constant. The fitting of this function to the experimental data gives a robust estimation of the lattice constant from the data, since all the measurement are taken into account simultaneously.

Fig. 4 shows the 2D plot of the fitted function to the experimental data.

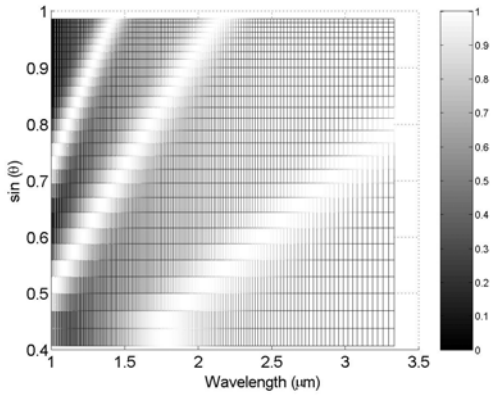

Fig. 4. 2D plot of the fitted function to the experimental data.

The results are summarized in table 1. A fairly good agreement of the lattice constant determined with the Bragg-diffraction measurements with the expected one has been obtained. The slight difference might be caused by the divergence of the beam, which results in wider diffraction peaks.

Table 1.

Lattice constant		
Lattice direction	GX	GM
Calculated	4,36 μm	2,98 μm
Expected	4 μm	2,83 μm

5. Conclusions

We have shown the feasibility of a technique to analyze the lattice properties of a 2D photonic crystal based on the measurement of Bragg-diffraction with a FT-IR spectrometer. A good agreement with the theoretical model and the measured data is obtained, although the determination of the lattice constant is affected by the beam divergence.

Acknowledgements

The authors thank T. Trifonov for the fabrication of the samples. This work was supported by the Spanish Commission of Science and Technology (CICYT) under grant number TEC2005-02038. Z. K. acknowledges the fellowship from the Universitat Rovira I Virgili. J. F. B. acknowledges the Ramon y Cajal fellowship from the Spanish Ministerio de Ciencia y Tecnología.

References

[1] E. Yablonovitch, "Inhibited spontaneous emission in solid state physics and electronics." Phys. Rev. Lett. **58**, pp. 2059-2062, May (1987).

[2] Kazuaki Sakoda, **"**Transmittance and Bragg reflectivity of two-dimensional photonic lattices." Phys. Rev. B, **52**, pp. 8992-9002, September (1995).

[3] Kazuaki Sakoda, Michihide Sasada, Tetsuya Fukushima, Akio Yamanaka, Noriko Kawai, and Kuon Inoue, „Detailed analysis of transmission spectra and Bragg-reflection spectra of a two-dimensional hotonic crystal with a lattice constant of 1.15 μm. ", J. Opt. Soc. Am. B, **16**, pp. 361-365, March (1999).